Tungsten mineralization during evolution of a magmatic–hydrothermal system: mineralogical evidence from the Xihuashan rare-metal granite in South China

Revision 2

JIE LI [1, 2], XIAO-LONG HUANG [1, *], QI FU [3], WU-XIAN LI [1]

[1] *State Key Laboratory of Isotope Geochemistry, Guangzhou Institute of Geochemistry, Chinese Academy of Sciences, Guangzhou 510640, China*

[2] *Key Laboratory of Submarine Geosciences, Second Institute of Oceanography, Ministry of Natural Resources, Hangzhou 310012, China*

[3] *Department of Earth and Atmospheric Sciences, University of Houston, Houston, TX 77204-5007, USA*

* Corresponding author: Xiao-Long Huang (e-mail: xlhuang@gig.ac.cn; Tel: +86-20-85290010; ORCID: 0000-0002-3138-986X)

ABSTRACT

Tungsten deposits are usually associated with granitic intrusions that record a long and complex evolution of the magmatic–hydrothermal system. However, the genetic link between magmatic–hydrothermal evolution and tungsten mineralization remains unclear. The Xihuashan tungsten deposit in South China, an important vein-type wolframite deposit, is closely associated with greisen and multiphase intrusive activity that produced biotite granite, two-mica granite, and muscovite granite. From the biotite granite to the two-mica granite to the muscovite granite, micas vary from siderophyllite to lithian siderophyllite, with decreasing K/Rb and Nb/Ta ratios and increasing Rb and Cs contents. The zoned micas in the muscovite granite and greisen display fluorine-depleted rims, reflecting subsolidus replacement by external aqueous fluids. The presence of siderite indicates a Fe, Mn and CO_2-rich fluid under reducing conditions. The micas in the greisen have higher F contents and lower Fe^{3+}/Fe^{2+} ratios than those in the muscovite granite, suggesting that the fluids contributing to greisen formation had a relatively high fluorine content and were reduced. The increase of CO_2 in the fluid enhanced its ability to unlock W from melts/rocks into fluids. The reducing environment also facilitated the tungsten mineralization. During greisenization, the pH value of the fluid increased, which destabilized the polymeric tungstates to form WO_4^{2-}. The mixture of W-rich solution and Fe, Mn-rich external fluid eventually precipitated as vein-type wolframite in favorable locations. An empirical equation ($Li_2O = 0.0748 \times F^2 + 0.0893 \times F$) was introduced for estimating the Li_2O contents of hydrothermal micas

using the F contents determined by EPMA.

Key words: rare-metal granite; tungsten mineralization; magmatic–hydrothermal evolution; mica; siderite; South China

INTRODUCTION

Most tungsten deposits are closely associated with granitic intrusions, and the styles of mineralization may be diverse, including quartz veins, stockworks, breccia, skarn, greisen, pegmatite, and porphyry. Wolframite-bearing quartz veins, regarded as an important type of hydrothermal deposit, commonly occur in differentiated granitic plutons that show varying degrees of hydrothermal alteration (e.g., Gleeson et al. 2001; Schaltegger et al. 2005; Vigneresse 2006). The relationship between magmatic–hydrothermal activities and tungsten mineralization is therefore a critical issue in understanding the formation of tungsten deposits. For individual deposits, the role of the intrusion as the main source of fluids and metals is usually unclear due to the multiple overprint/reopening of the veins and to the lack of geochronological data constraining the timing of magmatic and hydrothermal events. It has been proposed that the ore-forming elements may be concentrated during multiple stages of magmatic activity and then extracted by magmatic fluids (e.g., Che et al. 2013; Harlaux et al. 2018a), or be leached from granitoids and/or metamorphic rocks and transported by external (metamorphic or meteoric) fluids (e.g., Linnen and Williams–Jones et al. 1995; Vindel et al. 1995; Vallance et al. 2001). Most previous studies on the relationship between magmatic–hydrothermal episodes and tungsten mineralization have been based on the geochronology of deposits and their host granites (e.g., Wang et al. 2011; Li et al. 2013), experiments on partition coefficients between minerals and fluids/melts (e.g., Linnen and Cuney 2005; Che et al. 2013), analyses of fluid inclusions (e.g., Wei et al. 2012), and analyses of mineral geochemistry and stable isotopes (Legros et al. 2019). Although

recent studies have successfully dated wolframite from tungsten deposits (e.g., Harlaux et al. 2018b; Deng et al. 2019), limitations still exist, owing to the lack of suitable techniques for precisely dating both hydrothermal deposits and associated granitoids, the intrinsic differences between modeled and natural granitic systems, and uncertainties on whether fluid inclusions are representative of ore-forming fluids.

The textures and chemical compositions of ore-bearing oxide minerals, rock-forming minerals, and even accessory minerals may be used to track magmatic–hydrothermal processes in granitic systems and related metal mineralization (e.g., Roda–Robles et al. 2007; Van Lichtervelde et al. 2008; Yang et al. 2013; Li et al. 2015; Yin et al. 2019). Micas are ubiquitous minerals in peraluminous granitic systems, and these primary magmatic or secondary minerals (due to fluid interactions) have the potential to record the processes of fractional crystallization and hydrothermal evolution. As the major rock-forming mineral that hosts tungsten (e.g., 1.9−198 ppm in micas from peraluminous granites; Simons et al. 2017; El Korh et al. 2020), micas provide an effective proxy for tracing the progressive enrichment and ore-forming processes during magmatic–hydrothermal evolution (Legros et al. 2016, 2018; Yin et al. 2019). In addition to CO_2-rich fluid inclusions, carbonates (including synchysite, siderite, and calcite) may occur frequently in rocks associated with tungsten deposits, suggesting that the fluids involved in W-mineralization are enriched in CO_2 (Castorina and Masi 2008; Wei et al. 2012).

The widespread rare-metal deposits in South China are closely associated with Mesozoic granitic rocks, and an example is the Nanling W–Sn polymetallic

mineralization region (Fig. 1a) (Yin et al. 1995; Wang et al. 2003; Li et al. 2015). The Xihuashan tungsten deposit located in the Jiangxi Province is a typical vein-type wolframite deposit with minor Sn–Be mineralization (Nie and Wang 2007), and it is one of the major tungsten deposits in the world (Sinclair et al. 2014). The Xihuashan deposit is spatially and temporally associated with Jurassic granitic intrusions (Wang et al. 2011; Li et al. 2013; Yang et al. 2018), and it shows genetic links with the magmatic and hydrothermal evolution of the granitic intrusions. This deposit therefore provides an opportunity to investigate the mechanism of W enrichment and mineralization in rare-metal granites during the evolution of the magmatic–hydrothermal system. Previous studies on the Xihuashan deposit were focused mainly on the geochronology of the deposits and related granites (Wang et al. 2011; Guo et al. 2012; Hu et al. 2012; Li et al. 2013), fluid inclusions and wolframite formation (Wei et al. 2012; Huang et al. 2013), and magmatic fractionation or hydrothermal alteration of the granites (Le Bel et al. 1983; Maruéjol et al. 1990; Wang et al. 2003; Yang et al. 2013). This paper presents the results of whole-rock major and trace element analyses of the Xihuashan rare-metal granite as well as the chemical compositions of the micas and siderite, to elucidate the relationships between the tungsten mineralization and the magmatic–hydrothermal evolution of highly fractionated granitic melts, and to reveal the relative contributions of magmatic and hydrothermal processes to the formation of tungsten ore deposits. The results show the critical role of greisenizing fluids and magma fractionation in the tungsten mineralization, and provide new insights into the metallogenesis of tungsten in rare-metal granites.

GEOLOGICAL SETTING AND PETROGRAPHY

The South China Block (SCB) comprises the Yangtze Block in the northwest and the Cathaysia Block in the southeast (Fig. 1a). The two blocks were amalgamated during the early Neoproterozoic (e.g., Li et al. 2009; Zhao et al. 2011). During the Phanerozoic, the Cathaysia Block was subjected to intensive and widespread multiphase orogenesis and magmatism (Li et al. 2012). The igneous rocks of Jurassic and Cretaceous age are predominantly granites and rhyolites with subordinate mafic and rare intermediate lithologies (Zhou et al. 2006; Li et al. 2012). The Jurassic rocks occur over large parts of the Cathaysia Block, while the Cretaceous rocks cover the coastal area of SE China and the middle to lower reaches of the Yangtze River in the Yangtze Block (Fig. 1a). The majority of highly evolved and peraluminous granitic rocks were formed during the Jurassic with a few during the Cretaceous (Legros et al. 2020). These rocks in the Nanling area are associated with W–Sn–Mo–Bi–Be–Nb–Ta mineralization, and the area is well known as the Nanling tungsten–tin polymetallic mineralization region (NPMR, Fig. 1a) (e.g., Wang et al. 1982; Pei and Hong 1995).

The Xihuashan mining district is located in the southwestern part of the Jiangxi Province, South China (Fig. 1). It contains more than 700 economically viable ore veins, including W–Sn–Be mineralization (Nie and Wang 2007). There are six main tungsten mines in the district, namely Xihuashan, Dangping, Shenlongkou, Luokeng, Xialuogushan, and Niuzishi (Fig. 1b). The Xihuashan Mine hosts the largest vein-type wolframite deposit in the district, with the total estimate of WO_3 being 81,300 tons and

an average ore grade of 1.08 % WO_3 (Wei et al. 2012). The deposit is spatially and temporally related to a multiphase granitic intrusion that crops out over an area of about 20 km^2 (Guo et al. 2012). Previous geochronological studies indicated a close temporal relationship between the granitic magmatism and the W mineralization. For example, the crystallization ages of the major intrusions are 156–161 Ma (Guo et al. 2012; Li et al. 2013; Tang et al. 2020), and the Re–Os ages of molybdenites in the ore are identical (157 ± 3 Ma; Wang et al. 2011). The Xihuashan granitic complex was emplaced in upper Cambrian low-grade metamorphosed flysch-like sedimentary rocks, which underwent contact metamorphism (Le Bel et al. 1984). Wei et al. (2012) suggested the ore-forming fluids to be a mixture of magmatic and hydrothermal fluids derived from the granitic melts and meteoric water. With the knowledge obtained from geological mapping and exploratory drilling, the Xihuashan granitic complex may be divided into four successive intrusions (G1–G4; Fig. 1b) (Maruéjol et al. 1990; Wang et al. 2003). The G1 (coarse-grained biotite granite) occurs as the outermost part of the complex. The G2 (medium-grained biotite granite) hosts tungsten mineralization at the Xihuashan Mine. The G3 (medium- to fine-grained biotite granite) hosts tungsten mineralization at the Dangping Mine, whereas the G4 (fine-grained biotite granite) occurs as a barren border of G3.

The collected samples of G2 (medium-grained biotite granite) in the Xihuashan Mine include biotite granite, two-mica (lithian siderophyllite–muscovite) granite, muscovite granite, and greisen (Fig. 2a–d). The biotite granite crops out over an area of about 5.2 km^2. The greisen, two-mica granite and muscovite granite are only exposed in

the sub-surface and were investigated using drilled samples and exposure in the mine tunnels. Liu (2005) and Huang et al. (2006) showed that the greisen was usually associated with tungsten ore veins cutting the fine-grained two-mica granite, the muscovite granite, or the country rocks. There is a transition between the two-mica granite and the muscovite granite, both of which intruded the biotite granite (Liu 2005; Huang et al. 2006). The main accessory minerals of the Xihuashan intrusive rocks are fluorite, apatite, zircon, thorite, xenotime, and rutile (Supplementary Table 1).

The *biotite granite* consists of quartz (32–38%), K-feldspar (19–20%), plagioclase (32–34%), and siderophyllite (8–13%) (Fig. 2a). Plagioclase is subhedral or euhedral and shows compositional zoning. The siderophyllite grains are coarse and up to 2 mm in diameter. The plagioclase and siderophyllite alway host inclusions of ilmenite and apatite. Rutile is common as a secondary mineral associated with chloritization of the micas. The fluorite grains are anhedral and contain high yttrium contents (Y_2O_3 = 8–15 wt%). The accessory minerals enriched in REEs include apatite, monazite, allanite, and zircon.

The *two-mica (lithian siderophyllite–muscovite) granite* is composed mainly of quartz (30–35%), K-feldspar (14–15%), plagioclase (43–49%), and micas (6–8%) (Fig. 2b). The micas are dominantly lithian siderophyllite (~6%) with lesser amounts of muscovite (~2%). The primary mica crystals are coarse and up to 2 mm in size, while most secondary micas are fine-grained sericite within large plagioclase and K-feldspar phenocrysts. The lithian siderophyllite always contains inclusions of ilmenite and apatite, and the rims always show porosity due to dissolution. Xenotime is the principal

174 phosphate mineral in the two-mica granite, and other common accessory minerals are
175 zircon, garnet, and fluorite.

176 The *muscovite granite* consists of quartz (39–45%), K-feldspar (19–22%),
177 plagioclase (32–35%), and muscovite (~4%) (Fig. 2c). The accessory minerals include
178 spessartine, zircon, fluorite, xenotime, and siderite. The siderite crystals are anhedral
179 and elongate, and they occur mostly along the cleavages of the micas.

180 The *greisen* is composed of quartz (49–55%), lithian siderophyllite (30–35%), and
181 muscovite (9–11%) (Fig. 2d). The principal accessory minerals include zircon, xenotime,
182 fluorite, siderite, niobotantalates, and wolframite. Xenotime and zircon are the
183 predominant REE-rich minerals, while niobotantalates and wolframite are the
184 tungsten-bearing minerals.

185

186 ## ANALYTICAL METHODS

187 The whole rock geochemical analyses were carried out at the State Key Laboratory
188 of Isotope Geochemistry (SKLaBIG), Guangzhou Institute of Geochemistry (GIG),
189 Chinese Academy of Sciences (CAS). To eliminate potential contamination, samples
190 were cut into slabs and the central parts (> 200 g) were selected for whole-rock analyses.
191 The rocks were crushed into pieces with size of < 0.5 cm in diameter, cleaned with
192 deionized water in ultrasonic bath, and then pulverized in a corundum mill. Major
193 element oxides were determined using a Rigaku RIX 2000 X-ray fluorescence (XRF)
194 spectrometer. Samples were prepared as glass discs by a Rigaku desktop fusion machine,
195 mixing 0.50 g of rock powder (dried at 110 °C) with 4.0 g of $Li_2B_4O_7$ for 15 min at

196 1100 °C in 95% Pt - 5% Au crucibles. Calibration lines used for quantification were
197 produced by bivariate regression of data from 36 reference materials. Matrix corrections
198 were also incorporated into calibration using the empirical Traill-Lachance procedure.
199 For whole rock analyses, total Fe is reported as Fe_2O_3 (Supplementary Table 2). The
200 analytical uncertainty was between 1 % and 5 %. The additional quantitative analysis of
201 F was conducted by ALS Chemex (Guangzhou) Co Ltd., China, using the methods of
202 KOH fusion and ion selective electrode, or Na_2O_2 fusion, citric acid leach and ion
203 selective electrode. Analytical precision of F was lower than 10%.

204 Trace elements were determined using inductively coupled plasma-mass
205 spectrometry (ICP-MS). The rock powder was digested in a mixture of HF and HNO_3 in
206 high-pressure Teflon bombs. An internal standard solution containing single element Rh
207 was used to monitor signal drift. The detailed procedure was described in Li et al.
208 (2006). The US Geological Survey and Chinese National Standards, including SARM-4,
209 W-2, BHVO-2, AGV-2, GSR-1, GSR-2 and GSR-3, were used for calibration.
210 Analytical precision of REE and other incompatible elements was in the range of 1 to
211 5 %.

212 The siderites were examined using HORIBA Xplora laser Raman
213 microspectroscopy at the Key Laboratory of Mineralogy and Metallogeny (KLMM),
214 GIG-CAS. An Ar ion laser operated at 44 mW was used to produce an excitation line
215 with wavelength of 532 nm. The scanning range of spectra was set between 100 and
216 4000 cm^{-1} with an accumulation time of 10 s for each scan. The spectral resolution was
217 0.65 cm^{-1}. The Raman shift of a monocrystalline silicon piece was measured to be 520.7

This is the peer-reviewed, final accepted version for American Mineralogist, published by the Mineralogical Society of America.
The published version is subject to change. Cite as Authors (Year) Title. American Mineralogist, in press.
DOI: https://doi.org/10.2138/am-2020-7514. http://www.minsocam.org/

218 cm^{-1} before analyses.

219 Back-scattered-electron (BSE) images were obtained by a Zeiss Supra 55
220 field-emission scanning electron microscope (FE-SEM) at the SKLaBIG-GIG-CAS.
221 The *in-situ* mineral composition analyses were performed using the JEOL JXA8100
222 electron probe micro-analyzer (EPMA) at the SKLaBIG-GIG-CAS, with the operating
223 conditions of 15 kV accelerating voltage, 20 nA beam current and 1 μm beam size
224 (siderite) or 5 μm beam size (micas). A variable peak counting time of 7–40 s was
225 designed for the intensity of the characteristic X-ray lines and desired precision
226 (Supplementary Table 3). The raw data were corrected using ZAF correction. For micas,
227 the detection limits for most elements are lower than 251 ppm, and those for F and Rb
228 are 568 ppm and 631 ppm, respectively (Supplementary Table 3). Relative uncertainties
229 were estimated to be ca. 7% for F and 10–15 % (1σ) for Cl. Chemical formulae of micas
230 were calculated from mineral analyses based on 24 anions (O, F, OH), and Fe^{3+} was
231 estimated following the method by Lin and Peng (1994) described in Supplementary
232 Table 4. The CO_2 content in siderite was calculated by stoichiometry.

233 *In-situ* trace element concentrations were measured in mica and siderite grains
234 using an Agilent 7500a quadrupole ICP-MS coupled with a RESOlution M-50 laser
235 ablation system at the KLMM-GIG-CAS. The operating conditions included a spot size
236 of 42 μm, repetition rate of 5 Hz, maximum energy of 90 mJ and laser fluence of 7
237 J/cm^2. Argon was used as a make-up gas and mixed with helium as the carrier gas via a
238 cyclone mixer prior to entering the ICP torch. The National Institute of Standards and
239 Technology (NIST) 610 glass and 612 glass were used as external standards for quality

control (Jochum et al. 2011). Every analysis of six samples was followed by NIST 610 and 612 standards for time-dependent calibration of sensitivity drift. The internal standards are ^{27}Al and ^{57}Fe for mica and siderite, respectively. The off-line data processing was performed using the commercial software ICPMSDataCal 6.7 (Liu et al. 2008). The dwell time of each spot is 70 s of analysis time (30 s background, 40 s ablation). Limits of detection (LOD) were calculated using the 3σ criterion detailed by Longerich et al. (1996). The relative standard deviation (RSD) varies from 1% to 10%. More details on the standards are reported in Supplementary Table 5.

WHOLE-ROCK COMPOSITIONS

Eight samples (two of each rock type) were analyzed for their whole rock major and trace element compositions (Supplementary Table 2). The granite samples are all peraluminous (A/CNK = 1.02–1.10; Supplementary Table 2), with high SiO_2 (72.50–82.54 wt%), F (0.08–0.67 wt%), and alkali contents ($Na_2O + K_2O$ = 6.36–8.78 wt%) but low contents of MgO (0.02–0.38 wt%), Fe_2O_3 (0.44–2.02 wt%), and TiO_2 (<0.18 wt%). From the biotite granite to the two-mica granite to the muscovite granite, the TiO_2, MgO, P_2O_5, CaO, and F contents decrease gradually with decreasing Fe_2O_3 contents (Fig. 3), consistent with previous data reported by Guo et al. (2012). The two greisen samples display higher contents of SiO_2 (79.81–81.42 wt%) but lower contents of Al_2O_3 (8.98–9.74 wt%), MgO (0.06–0.09 wt%), MnO (0.15–0.19 wt%), TiO_2 (0.02–0.03 wt%), CaO (0.21–1.64 wt%), and alkalis ($Na_2O + K_2O$ = 3.37–3.38 wt%) than the granite samples (Supplementary Table 2; Fig. 3). The greisen samples have high Fe_2O_3 (3.28–3.36 wt%)

This is the peer-reviewed, final accepted version for American Mineralogist, published by the Mineralogical Society of America.
The published version is subject to change. Cite as Authors (Year) Title. American Mineralogist, in press.
DOI: https://doi.org/10.2138/am-2020-7514. http://www.minsocam.org/

and F (1.05–1.22 wt%) contents (Fig. 3), due to abundant lithian siderophyllite, wolframite, and fluorite.

The granite and greisen samples have a narrow range of REE concentrations (80.4–129 ppm; Supplementary Table 2) and similar chondrite-normalized REE patterns with strong negative Eu anomalies (Eu/Eu* = 0.01–0.31) and a weak lanthanide tetrad effect, consistent with previous data reported by Guo et al. (2012) (Fig. 4a). The $[La/Yb]_N$ and Eu/Eu* values decrease following the sequence of biotite granite, two-mica granite, muscovite granite, and greisen. The muscovite granite and greisen are depleted in LREEs and Eu, but enriched in HREEs, and this differs from the typical "wing-shaped" REE patterns for highly evolved granites (Irber 1999; Li et al. 2015). In the multi-element diagrams normalized to the mean composition of upper continental crust, all the samples are enriched in Cs (11.1–73.5 ppm), Rb (312–1020 ppm), W (4.82–65.3 ppm), Ta (3.35–27.2 ppm), Sn (5.65–198 ppm), and Li (37.8–987 ppm), but depleted in Ba (3.31–266 ppm), Sr (1.31–90.6 ppm), P (9.29–204 ppm), and Ti (12.1–1069 ppm) (Fig. 4b). Overall, the muscovite granite and greisen have much higher Li, Cs, Rb, and Sn abundances but lower Ba, Sr, and P than the biotite granite and two-mica granite.

MINERAL COMPOSITIONS

Mica

Most micas in the biotite granite and two-mica granite are homogeneous in their chemical compositions, but those in the muscovite granite and greisen show

This is the peer-reviewed, final accepted version for American Mineralogist, published by the Mineralogical Society of America.
The published version is subject to change. Cite as Authors (Year) Title. American Mineralogist, in press.
DOI: https://doi.org/10.2138/am-2020-7514. http://www.minsocam.org/

284 compositional zoning with distinct core and rim on BSE images or have a porous rim
285 due to dissolution (Fig. 5). A total of 267 EPMA analyses were performed on eight
286 samples, along with 76 LA–ICP–MS analyses on the same spots previously analyzed by
287 EPMA. Altogether, these analyses cover all the rock types in the pluton and different
288 areas of compositionally zoned mica grains (Supplementary Table 6).

289 The micas in the Xihuashan pluton show a wide range of elemental compositions.
290 Siderophyllite in the biotite granite has the highest contents of FeO^{Tot} (21.70–24.57 wt%,
291 2.757–3.253 apfu), TiO_2 (0.53–3.20 wt%, 0.061–0.373 apfu), and MgO (3.96–5.12 wt%,
292 0.925–1.165 apfu) of all the micas, but the lowest contents of SiO_2 (34.44–37.00 wt%,
293 5.469–5.667 apfu) and Al_2O_3 (16.34–20.77 wt%, 2.333–2.531 apfu) (Fig. 6;
294 Supplementary Table 6). In the two-mica granite, the lithian siderophyllite has higher
295 contents of FeO^{Tot} (19.40–23.17 wt%, 2.439–3.002 apfu) and TiO_2 (0.03–1.57 wt%,
296 0.004–0.183 apfu) than the muscovite (FeO^{Tot} = 5.00–8.85 wt%, 0.576–1.051 apfu;
297 TiO_2 = 0.01–0.40 wt%, 0.001–0.042 apfu). Micas in the muscovite granite and greisen
298 have lower contents of FeO^{Tot} (3.43–19.97 wt%, 0.388–2.504 apfu), TiO_2 (below the
299 detection limit to 0.51 wt%, bdl.–0.058 apfu), and MgO (0.04–0.70 wt%, 0.008–0.147
300 apfu), but higher contents of SiO_2 (37.77–47.99 wt%, 5.683–6.529 apfu) than those in
301 the biotite granite and two-mica granite (Fig. 6). Micas in the biotite granite, two-mica
302 granite, and muscovite granite have similar F contents, all of which are lower than the
303 value of the cores of greisen micas (Fig. 6). Micas in all samples have extremely low Cl
304 contents (mostly less than 0.06 wt%), which decrease roughly from siderophyllite,
305 lithian siderophyllite, and muscovite along with a negative correlation with SiO_2

306 contents (Fig. 6f).

307 Micas in the biotite granite have much higher V, Sc, Cr, Co, and Ni contents than
308 the micas in other rocks (Fig. 7a; Supplementary Table 6). Overall, the micas in the
309 Xihuashan pluton have high contents of Rb, Cs, Nb, and Ta (typically Rb > 1000 ppm,
310 Cs > 200 ppm, Nb > 20 ppm, Ta > 10 ppm) but the contents of most REEs are below
311 detection limits (Supplementary Table 6). The lithian siderophyllites in the two-mica
312 granite and the cores of micas in the muscovite granite and greisen have higher Rb and
313 Cs contents than siderophyllites in the biotite granite (Fig. 7b, c), while the Nb and Ta
314 contents of micas increase from the biotite granite to the two-mica granite, but decrease
315 slightly in the greisen (Fig. 7d, e). Micas in the muscovite granite and greisen have
316 lower Nb/Ta ratios (0.84–5.63) than siderophyllites in the biotite granite and lithian
317 siderophyllites in the two-mica granite (Nb/Ta = 1.77–17.15) (Fig. 7f). The Sn and W
318 contents of micas in the analyzed samples increase gradually from the biotite granite to
319 the two-mica granite and to the cores of micas in the muscovite granite.

320 The micas in the muscovite granite and greisen generally exhibit core–rim
321 zonation on BSE images (Fig. 5). The cores of zoned micas in the muscovite granite and
322 greisen commonly have lower SiO_2 (37.77–42.47 wt%, 5.683–6.333 apfu) and Al_2O_3
323 (23.33–26.91 wt%, 1.667–2.317 apfu) contents but higher FeO^{Tot} (11.32–19.97 wt%,
324 1.356–2.504 apfu), Li_2O (0.26–1.74 wt%, 0.141–1.023 apfu), F (0.73–4.26 wt%, 0.342–
325 1.981 apfu), Rb (4753–5860 ppm), Cs (377–1691 ppm), Ta (15.8–171 ppm), and Nb
326 (33.9–195 ppm) contents than the rims (Figs 5, 6e, 7b–e; Supplementary Table 6). The
327 cores of zoned micas in the muscovite granite and greisen have lower Nb/Ta ratios

328 (0.97–1.55 and 0.84–2.14, respectively) than the rims (1.29–5.63 and 2.01–3.40) (Fig.
329 7f). In addition, the mica cores in the muscovite granite have higher W (70–84 ppm) and
330 Sn (694–848 ppm) contents than the rims (14.9–63 ppm and 265–694 ppm,
331 respectively). The zoned micas in the greisen samples exhibit an increasing trend of W
332 and Sn from core to rim, with values higher than the rims of zoned micas in the
333 muscovite granite (Fig. 7g, h).
334
335 **Siderite**
336 All the siderites in the muscovite granite and greisen samples occur along the
337 cleavages or the crystal borders of zoned micas (Fig. 5), which were most likely formed
338 as secondary minerals due to the presence of CO_2-rich hydrothermal fluids (Buckley
339 and Woolley 1990). The siderites were identified using Raman spectroscopy and EPMA.
340 The Raman spectrum of the investigated mineral shows a strong intensity band at
341 1081.73 cm^{-1} and a low intensity band at 276.97 cm^{-1} (Fig. 8), corresponding to the
342 symmetric stretching and external vibration of the CO_3 group, respectively, which are
343 consistent with the characterization of carbonates reported by Buzgar and Apopei
344 (2009). Minor shifts in position may be due to the effect of natural impurities in the
345 studied samples. The siderites have high contents of FeO (30.14–56.01 wt%), MnO
346 (3.47–20.39 wt%), and CO_2 (35.29–37.60 wt%), but low contents of MgO (<0.22 wt%)
347 and alkalis ($Na_2O + K_2O < 1$ wt%) (Supplementary Table 7). The siderites in the
348 muscovite granite have higher REE contents (ΣREE = 62–109 ppm) than those in the
349 greisen (ΣREE = 6.92–34.4 ppm; Supplementary Table 8). They show chondrite

normalized LREE-depleted and HREE-enriched pattern with very low values of $[La/Yb]_N$ (0.01–0.05) (Fig. 8c; Supplementary Table 8) and strongly negative Eu anomalies (Eu/Eu* < 0.32; Fig. 8c; Supplementary Table 8). On the multi-element diagram normalized to average upper continental crust, the siderites are enriched in Li, Rb, Cs, Ta, W, and Sn, but depleted in Ba, Zr, and Ti, similar to the whole rock composition (Fig. 8d).

DISCUSSION

Estimation of lithium contents in micas

The Li_2O content of mica may be measured directly by LA–ICP–MS or estimated by EPMA from empirical equations based on the crystallochemical relationship between Li and other major elements in the mica. Considering the different beam sizes of the LA–ICP–MS (e.g., 42 μm) and EPMA (e.g., 1 μm) methods, the Li_2O content of mica estimated from the EPMA results using empirical equations may provide a better constraint on the compositional variation at the micrometer scale.

The micas in the Xihuashan pluton display two trends on the diagram of SiO_2 versus Li_2O with contents measured by LA–ICP–MS (Fig. 9a). Siderophyllites in the biotite granite and lithian siderophyllites in the two-mica granite have relatively low SiO_2 contents that show a positive correlation with Li_2O (Fig. 9a), which is consistent with the regression function between Li_2O and SiO_2 (Fig. 9a) for trioctahedral micas (Tischendorf et al. 1997):

$$Li_2O = 0.289 \times SiO_2 - 9.658 \quad (1)$$

This is the peer-reviewed, final accepted version for American Mineralogist, published by the Mineralogical Society of America.
The published version is subject to change. Cite as Authors (Year) Title. American Mineralogist, in press.
DOI: https://doi.org/10.2138/am-2020-7514. http://www.minsocam.org/

372 In contrast, muscovites in the two-mica granite and micas in the muscovite granite and
373 greisen have relatively higher SiO_2 contents that show a negative correlation with Li_2O
374 contents (Fig. 9a). In particular, muscovites in the two-mica granite and the cores of
375 micas in the muscovite granite show good correlation with the regression function
376 between Li_2O and F (Fig. 9b) for dioctahedral micas (Tischendorf et al. 1997):

377 $$Li_2O = 0.3935 \times F^{1.326} \quad (2)$$

378 while micas in the greisen samples clearly deviate from this function (Fig. 9b). The Li
379 contents of hydrothermal micas (e.g., micas in the greisen) appear to be overestimated
380 using Eq. (2) for dioctahedral micas (Fig. 9b). While the equations in Tischendorf et al.
381 (1997) were designed for magmatic systems, additional adjustment is required for
382 application to hydrothermal systems (Legros et al. 2016). In this paper, a new empirical
383 equation for the Li_2O and F contents of hydrothermal micas is introduced (Fig. 9c):

384 $$Li_2O = 0.0748 \times F^2 + 0.0893 \times F \quad (3)$$

385 This equation may be used for estimating the Li_2O content of hydrothermal mica from
386 the F content determined by EPMA. The Li contents calculated with this equation are in
387 agreement with the values measured by LA–ICP–MS ($R^2 = 0.82$) (Fig. 9d).

388 The Li_2O contents determined using EPMA indicate that the biotites in the biotite
389 granite and two-mica granite are siderophyllite and protolithionite (lithian
390 siderophyllite), respectively, which is consistent with the trend of magmatic evolution
391 (Fig. 10). Lithian siderophyllites in the greisen have higher Li_2O contents (1.57–1.74
392 wt%) than those in the two-mica granite (0.88–1.33 wt%). They are protolithionites
393 following the classification proposed by Tischendorf et al. (1997) (Fig. 10a).

Alternatively, they belong to the transitional series between dioctahedral and trioctahedral micas based on Foster (1960) (Fig. 10b), also termed the ferrous aluminum micas in Monier and Robert (1986). Muscovites in the two-mica granite, muscovite granite, and greisen all belong to the transitional series, but in their octahedral sites they have lower contents of Li_2O and divalent metal cations (Fe^{2+}, Mn^{2+}, Mg^{2+}) than the lithian siderophyllites in the greisen (Fig. 10b).

Variation of halogens in the melts and fluids

The micas display a wide range of F contents (0.41–4.26 wt%). Overall, the siderophyllites in the biotite granite have the lowest F contents (0.84–1.95 wt%), while micas in the greisen have the highest (up to 4.26 wt%). The cores of zoned micas in the muscovite granite and greisen typically have higher F contents (0.73–4.26 wt%) than the rims (0.41–3.46 wt%) (Supplementary Table 6). In addition, the micas have much lower Cl contents (up to 0.06 wt%) than F (0.41–4.26 wt%; Supplementary Table 6). Indeed, the substitution of Cl into the OH site of mica is much less favorable than the substitution of F (Munoz 1992), due to the significantly larger ionic radius of Cl^- (1.81 Å; cf. F^- = 1.31 Å and OH = 1.38 Å).

The exchange of F, Cl, and OH between micas and associated fluids may be used to obtain the halogen fugacity of the fluids (Munoz 1984) as well as the halogen concentrations in the melt (Zhang et al. 2012). Since the measured Cl contents of the Xihuashan micas are extremely low (mostly less than 0.06 wt%, with large errors of 10%–15%), the exchange of Cl and OH between micas and associated fluids is not

416 further discussed.

417 The equations used for estimating the F fugacity of a fluid [log(fH$_2$O/fHF)] and
418 the F concentration in a melt (W_F^m) are listed as follows (Munoz 1984; Zhang et al.
419 2012):

420 $$\log\left(\frac{fH_2O}{fHF}\right) = \frac{1000}{T} \times \left(2.37 + 1.1X_{Mg}\right) + 0.43 - \log(\frac{X_F}{X_{OH}})^{mica} \quad (4)$$

421

422 $$W_F^m = \frac{1}{1+\frac{fH_2O}{fHF}} \times \frac{19}{18.02} \times \frac{10^6}{0.000943 \times T - 0.574} \quad (5)$$

423 where X_F and X_{OH} are the mole fractions of F and OH in the hydroxyl site of mica,
424 respectively, X_{Mg} is the mole fraction of Mg in the octahedral site of mica, and T is the
425 crystallization temperature of mica in degrees Kelvin. Due to the difficulties in
426 calculating the crystallization temperatures of micas directly, the homogenization
427 temperatures of fluid inclusions (Mu et al. 1982; Zhang et al. 1982; Wei et al. 2011) and
428 melt inclusions (Chang and Huang 2002) in the Xihuashan tungsten deposit were
429 adopted to estimate the F fugacity of the fluids and the F content of the melt. The melt
430 inclusions in beryl from the wolframite–quartz veins in the Xihuashan tungsten deposit
431 gave a homogenization temperature of 720 °C (Huang et al. 2006), consistent with the
432 mean value (703 ± 28 °C; range of 643 to 890 °C) of the temperature given by the
433 Ti-in-zircon thermometer for the Xihuashan granites (Yang et al. 2018), which can be
434 regarded as the crystallization temperature of the Xihuashan granitic magma. In addition,
435 there were two generations of fluid in the Xihuashan granites, based on stable oxygen
436 isotope data from fluid inclusions (Mu et al. 1982; Zhang et al. 1982; Wei et al. 2011).
437 The primary ore-fluid had a temperature of 370 ± 30 °C (fluid of magmatic origin, δ^{18}O

This is the peer-reviewed, final accepted version for American Mineralogist, published by the Mineralogical Society of America.
The published version is subject to change. Cite as Authors (Year) Title. American Mineralogist, in press.
DOI: https://doi.org/10.2138/am-2020-7514. http://www.minsocam.org/

= 10‰–13‰) and the late fluid had a temperature of 220 ± 10 °C (meteoric water, $\delta^{18}O$ = –8.7‰ to +3.1‰). It is assumed that the primary ore-fluid was related to the formation of the cores of zoned micas in the greisen and that the late fluid was related to the rims of zoned micas in the muscovite granite and greisen, and this will be discussed later. The results of calculations using Eq (4) and Eq (5) are given in Supplementary Table 6 and shown on Fig. 11. Overall, the $\log(fH_2O/fHF)$ values of the fluid decrease from the greisen (4.15–4.65, mean = 4.33) to the biotite granite (3.95–4.42, mean = 4.14) to the two-mica granite (3.38–3.82, mean = 3.65), and to the muscovite granite (3.26–3.91, mean = 3.56) (Fig. 11a). In general, F is preferentially concentrated in a residual melt when the volatiles of a hydrous magma are exsolved (Zhu and Sverjensky 1992). The loss of volatiles from a hydrous magma will enhance the F content in the residual melt, producing a lower OH/F value in the melt but a higher OH/F ratio in the associated fluid. This implies that the F content (W_F^m values) of the melt increases gradually from the biotite granite to the two-mica granite, and to the muscovite granite (Fig. 11c).

With regard to the zoned micas in the muscovite granite and greisen, the fluids related to the rims always have higher $\log(fH_2O/fHF)$ values than those related to the cores (Fig. 11a). In addition, the rims of micas in the muscovite granite and greisen all have higher Fe^{3+}/Fe^{2+} ratios than the cores (Fig. 11b). As the Fe^{3+}/Fe^{2+} ratio shows a positive correlation with temperature (Wones and Eugster 1965), the higher Fe^{3+}/Fe^{2+} ratios of the rims of zoned micas cannot be attributed to lower temperatures relative to the magmatic cores, but an increasing oxygen fugacity and H_2O content.

460

461 **Magmatic evolution of the Xihuashan intrusive rocks**

462 The Xihuashan granites have extremely variable whole-rock and mineral
463 compositions, indicating that the rocks might have undergone varying degrees of
464 fractional crystallization.

465 The micas show a wide range of compositions (Fig. 10) from siderophyllite to
466 lithian siderophyllite, which corresponds to the evolution of the magma from the biotite
467 granite to the two-mica granite. As a peraluminous melt system evolves, Rb and Cs are
468 compatible in biotite while Y, Th, and REEs are incompatible (Bea et al. 1994). The
469 micas in our samples have low Y, Th, and REE contents but extremely high Rb and Cs
470 contents (Supplementary Table 6), suggesting that fractionation of the micas was
471 insignificant during the magmatic evolution. The increase of Rb and Cs contents with
472 decreasing K/Rb ratios from the biotite granite to the two-mica granite (Fig. 12a, b)
473 further excludes the possibility of significant mica fractionation during the magmatic
474 evolution of the Xihuashan intrusive rocks. With regard to the feldspars, Rb and Cs are
475 compatible in K-feldspar but incompatible in plagioclase (Bea et al. 1994), and an
476 increase of Rb and Cs in micas from the biotite granite to the two-mica granite (Fig. 7b,
477 c) could be attributed to a remarkable fractionation of plagioclase. It is also consistent
478 with the fact that our samples are notably enriched in Li, Rb, and Cs compared with
479 upper continental crust (UCC) (Fig. 4b). In addition, xenotime rather than apatite is the
480 principal phosphate mineral in Ca-poor peraluminous granitic melts (Wang et al. 2003).
481 In the Xihuashan pluton, the two-mica granite and muscovite granite samples contain

abundant xenotime with apatite being absent or rare, which indicates an essentially Ca-poor peraluminous melt. The Ca-poor melt would have been the product of the fractional crystallization of Ca-rich minerals, including apatite and plagioclase. However, apatite fractionation, if it existed, could not have been primarily responsible for producing the Ca-poor peraluminous melt, because it would have required a large amount of phosphorus to exhaust the Ca in the system. Therefore, the presence of abundant xenotime in the two-mica granite and muscovite granite may provide evidence for plagioclase fractionation during the magmatic evolution, which is consistent with decreasing MgO, TiO_2, Fe_2O_3 and CaO (Fig. 3) and gradually pronounced Eu negative anomalies (Fig. 4a) from biotite granite to two-mica granite to muscovite granite.

Collectively, the variations in composition of mica in the Xihuashan pluton are consistent with a trend of magmatic evolution from the biotite granite to the two-mica granite to the muscovite granite. This evolutionary process was controlled mainly by the fractional crystallization of plagioclase.

The hydrothermal evolution recorded in zoned micas and siderite

Micas in highly evolved granites and pegmatites always show compositional zoning as a result of the evolution of the magma or sub-solidus fluid interactions (Roda–Robles et al. 2007; Van Lichtervelde et al. 2008; Li et al. 2015). Volatile components (e.g., H_2O, F, B, and P) and lithophile rare metal elements (e.g., Li, Rb, Cs, Ta, Nb, Sn, and W) are incompatible in major rock-forming minerals during the evolution of peraluminous melt systems. Accordingly, the Li_2O, F, Rb, Cs, Nb, and Ta

504 contents of mica may increase with the progressive evolution of the magma (Roda–
505 Robles et al. 2007), leading to differences in brightness in the zoning textures revealed
506 by the BSE images (Fig. 5). Since fluorine is concentrated in the melt during the
507 differentiation of a granitic melt when there is lack of fractionation of fluorine-enriched
508 minerals such as apatite and mica (Li et al. 2015), the supercritical fluids exsolved from
509 a highly fractionated Sn–W granitic magma are usually enriched in F (Thomas et al.
510 2005). The addition of F into the melt may increase the abundance of non-bridging
511 oxygens (NBOs), which increases the proportion of WO_4^{2-} tetrahedra in silicate melt.
512 Indeed, with our samples, the log(fH$_2$O/fHF) values decrease and the W_F^m values
513 increase from the biotite granite to the two-mica granite and the muscovite granite (Fig.
514 11), consistent with an evolution of magma without involvement of any notable
515 fractionation of apatite or mica. However, the rims of the zoned micas in the muscovite
516 granite and greisen have lower Li_2O, Rb, Cs, Nb, Ta, and F contents but higher Si and
517 Al contents than the cores (Fig. 9; Supplementary Table 6). Moreover, the rims of the
518 zoned micas belong to the transition series (Fig. 10), similar to the ferrous aluminum
519 micas described by Monier and Robert (1986), which were the products of metasomatic
520 alteration. Altogether, the characteristics of the compositional zoning and dissolution
521 textures (Fig. 5) of the micas in our samples indicate that they were produced by fluid–
522 rock interactions rather than melt differentiation. Furthermore, the micas would have
523 been enriched in F when they interacted with supercritical fluids exsolved from a highly
524 differentiated magma. The rims of the zoned micas show significant depletion in F
525 (Supplementary Table 6), corresponding to higher log(fH$_2$O/fHF) values than the mica

526 cores, and this suggests a process of subsolidus replacement by a dominantly external
527 aqueous fluid.

528 The siderites have variable REE contents (ΣREE = 6–110 ppm; Supplementary
529 Table 8) and negative Eu anomalies, which would have been caused by the fluids
530 having variable REE contents or pH values (Michard 1989; Möller et al. 2004). In
531 general, the total REE content of hydrothermal solutions increases with decreasing pH
532 values (Michard 1989; Möller et al. 2004). In acidic solutions, LREEs are likely to be
533 enriched in aqueous phases, while HREEs are preferentially adsorbed on mineral
534 surfaces (Schwinn and Markl 2005). Thus, siderites precipitated from fluids with
535 variable pH values would have variable LREE/HREE ratios. The siderites in our
536 samples of muscovite granite and greisen have similar $(La/Yb)_N$ ratios. Instead, different
537 sources of fluid with variable REE contents are more likely to have been responsible for
538 the wide range of REE contents that characterizes the siderites, and this is consistent
539 with the $\log(fH_2O/fHF)$ values of the rims of zoned micas in the greisen being generally
540 lower than those in the muscovite granite (Fig. 11).

541 The stability of siderite depends on the CO_2 fugacity and the oxygen fugacity
542 (Fusswinkel et al. 2013). Siderite is stable under conditions of low oxygen fugacity (i.e.,
543 $fO_2 = -38$ to -54) and high CO_2 fugacity (i.e., $fCO_2 = -1$ to $+2$) (Fusswinkel et al. 2013).
544 It is replaced by magnetite in the reaction "6 Siderite + O_2 = 2 Magnetite + 6 CO_2"
545 when the oxygen fugacity increases or the activity of CO_2 decreases (Hovis et al. 1991).
546 The lack of magnetite in the muscovite granite and greisen (Table 1) may be attributed
547 to a relatively reducing environment where the siderite crystals were stable. Therefore,

548 the presence of siderite in the Xihuashan granite indicates a reducing environment
549 during the fluid–rock interactions, and the oxygen fugacity (fO_2) would have been close
550 to the value constrained by the "$C + O_2 = CO_2$" buffer (Yang et al. 2013).

551 The fluids associated with the tungsten mineralization would have been of
552 external origin or exsolved from the melt (e.g., Wang et al. 2003; Wei et al. 2012;
553 Harlaux et al. 2018). It is noteworthy that the cores of zoned micas in the greisen and
554 muscovite granite show much lower log(fH_2O/fHF) values and Fe^{3+}/Fe^{2+} ratios than the
555 rims (Fig. 11), and this indicates that the fluids associated with the formation of the
556 greisen and muscovite granite had a higher fluorine fugacity and were even more
557 reducing than the fluids associated with the fluid–rock interactions. Such fluids might
558 have been supercritical fluids exsolved from the highly fractionated magma, and this is
559 consistent with the observation that the log(fH_2O/fHF) values associated with the cores
560 of micas in the greisen are close to those associated with magmatic micas in the granite
561 samples (Fig. 11a, b). In addition, based on the fluid inclusion studies, Wei et al. (2012)
562 proposed that a mixture of fluids from two different sources could have been
563 responsible for the deposition of wolframite in the Xihuashan deposit. Fluids with a low
564 oxygen fugacity and enriched in fluorine may be derived from fluid oversaturation of a
565 granitic melt (Maruejol et al. 1990; Wang et al. 2003), which may contribute to the
566 formation of the cores of zoned micas in the greisen and muscovite granite. The
567 fluid-rock interactions, however, involved mainly meteoric fluids that were associated
568 with alteration of early Li-rich micas into late muscovite (Legros et al. 2016). These
569 fluids were also enriched in H_2O and CO_2, as recorded in the rims of zoned mica and the

570 siderite in the greisen and muscovite granite. In particular, the rims of zoned micas in
571 the greisen samples have lower log(fH_2O/fHF) values than those in the muscovite
572 granite samples, which further indicates that the fluids associated with the greisen
573 contained larger amounts of magma-derived fluids.
574
575 **Tungsten enrichment during the evolution of the magmatic–hydrothermal system**
576 Tungsten deposits are usually associated with fractionated granitic magmas and
577 hydrothermal processes (e.g., Xie et al. 2016; Breiter et al. 2017). In peraluminous
578 granitic systems, tungsten commonly behaves as an incompatible element for most
579 rock-forming minerals and accumulates in melts during fractional crystallization
580 (Hulsbosch et al. 2016). The WO_3 content of columbite-group minerals increases from 5
581 to 15 wt% during magma evolution (Xie et al. 2018), which confirms that tungsten can
582 be concentrated in melts. In addition, mica may be used as an indicator of ore-forming
583 potential for tungsten granites (Yin et al. 2019). In the Xihuashan granite, the tungsten
584 content of micas increases from the biotite granite (0.36–12.8 ppm) to the muscovite
585 granite (14.9–84.1 ppm) while the K/Rb ratio of micas decreases (Fig. 12c), consistent
586 with the trend of magma evolution. However, magmatic wolframite can crystallize
587 directly from a highly evolved granite melt under restricted conditions, as for example
588 from a peraluminous melt with high concentrations (6 wt%) of fluxing compounds (B,
589 Li, F, and P) and with crystallization temperatures lower than 550 °C at 800 bars (Che et
590 al. 2013). In most cases, the required conditions for saturation of magmatic wolframite
591 cannot be reached in granitic melts due to the low levels of fluxing compounds. It is rare

592 to have a wolframite of purely magmatic origin, and hydrothermal fluids typically play
593 a significant role in W mineralization. In the Xihuashan granite, the lack of wolframite
594 in the muscovite granite suggests that the tungsten concentration in the melts did not
595 become saturated relative to wolframite as a result of magmatic fractionation. Indeed,
596 the whole-rock content of W in the Xihuashan granite (4.82–65.3 ppm) is much lower
597 than the solubility of wolframite in peraluminous granitic melts (~1000 ppm WO_3 at
598 750–800 °C; Štemprok 1990). Therefore, although tungsten may be concentrated in a
599 melt via magmatic fractionation, in the magmas of the Xihuashan pluton the W contents
600 were always much lower than the oversaturation level during the evolution of the
601 magma.

602 Hydrothermal activities may play an important role in W mineralization (e.g.,
603 Štemprok 1990; Li et al. 2018). The wolframite crystals in the greisen are intergrown
604 with zoned mica (Fig. 5d), and they would have formed during hydrothermal activity.
605 However, wolframite is absent from the muscovite granite, even though the abundant
606 zoned micas with dissolution textures (Fig 5a, b) provide evidence of fluid alteration.
607 The rims of zoned micas in the muscovite granite have lower W contents than the cores
608 (Fig. 7f), which was probably due to hydrothermal alteration. The hydrothermal fluids
609 liberated W from the micas and resulted in formation of a W-depleted rim, whereas W
610 was concentrated in the hydrothermal fluid. The elevated CO_2 concentration may
611 increase the acidity of fluid and the solubility of tungstates, which facilitates
612 concentrating W in the fluids (Liu et al. 2017; Wang et al. 2020). The rims of zoned
613 micas in the greisen have higher W contents than those in the muscovite granite (Fig.

This is the peer-reviewed, final accepted version for American Mineralogist, published by the Mineralogical Society of America.
The published version is subject to change. Cite as Authors (Year) Title. American Mineralogist, in press.
DOI: https://doi.org/10.2138/am-2020-7514. http://www.minsocam.org/

614 7f), which was probably due to different CO_2 and W concentrations in the hydrothermal
615 fluids. The W-rich rims of zoned mica in the greisen clearly show the involvement of
616 W-rich fluids in the formation of the tungsten deposit (Figs 5d, 7h). Furthermore, a fluid
617 rich in F, Li, and rare metals can induce greisenization in the upper part of the granitic
618 cupola, causing dissolution of feldspars and crystallization of new quartz, zinnwaldite,
619 fluorite, and topaz (Breiter et al. 2017). Greisenization consumes H^+ and increases the
620 pH value of fluids following the reaction:

$$2Na[AlSi_3O_8] + K[AlSi_3O_8] + 2H^+ = KAl_2[AlSi_3O_{10}](OH)_2 + 6SiO_2 + 2Na^+$$

621 Albite K-feldspar Muscovite Quartz

622 An increase in fluid pH during greisenization will destabilize the polymeric
623 tungstates to form WO_4^{2-} and other monomeric tungstates (Wang et al. 2020), which
624 may interact with metal cations (i.e., Fe, Mn or Ca) to form wolframite or scheelite.
625 Thus, greisenization promoted the generation of WO_4^{2-} in the fluids, and potentially
626 contributed to the formation of tungsten deposit (Audéta et al. 2008; Harlaux et al.
627 2017; Legros et al. 2019).

628

629 **IMPLICATIONS FOR TUNGSTEN MINERALIZATION**

630 The hydrothermal fluid related to the W deposits would have different sources,
631 including an early magmatic fluid and a later metamorphic or meteoric fluid (Wei et al.
632 2012; Hulsbosch et al. 2016). However, the signature of the early magmatic fluid is
633 usually overprinted by the metamorphic or meteoric fluid (Wei et al. 2012; Hulsbosch et
634 al. 2016). Thus, attempts to determine whether a magmatic or metamorphic fluid was

635 responsible for W mineralization associated with a granite typically provide
636 inconclusive results. In the Xihuashan tungsten granite, the composition and zoning
637 texture of micas may provide some valid constraints on the nature of fluids and the
638 mechanism for precipitation of wolframite. The interaction between external aqueous
639 fluids and pre-existing micas has played an important role in leaching the ore-forming
640 elements (i.e., W and Fe) from the micas into the fluids, which is proved by remarkably
641 dropped concentrations of W and Fe from the cores to the rims of zoned micas in the
642 muscovite granite (Figs 6c, 7h). The W-rich rims of the zoned mica in the greisen,
643 together with the high whole-rock F contents (up to 1.22 wt%) of greisen samples,
644 demonstrate that the fluid related to the greisenization was enriched in F and W. The
645 F-rich fluids involved in the greisenization were most likely derived from the
646 oversaturation of a rare-metal granitic melt (Maruéjol et al. 1990; Launay et al. 2018;
647 Legros et al. 2018). Therefore, the rims of zoned mica in the greisen are enriched in W
648 due to the effect of W-rich fluids, whereas the rims of zoned mica in the muscovite
649 granite are related to the dominant external fluids that had much lower W contents. This
650 difference between the zoned micas in the greisen and muscovite granite indicates that
651 the process of greisenization was critical for extracting and transporting the W from the
652 melts/rocks into the fluids (Launay et al. 2018).

653 The processes identified in the Xihuashan tungsten granite may have been active
654 in many wolframite-bearing quartz-vein deposits elsewhere. Some famous metallogenic
655 provinces or plutons, such as the French Massif Central, the Erzgebirge, the northern
656 Canadian Cordillera, Iberian Massif and the Nanling and Dahutang mineralization

657 regions in South China, are closely related to magmatic and hydrothermal processes
658 (e.g., Legros et al. 2016, 2018; Breiter et al. 2017a, b; Legro et al. 2016, 2018; Xie et al.
659 2018; Yin et al. 2019). Furthermore, the micas in these tungsten-bearing granites are
660 commonly zoned and enriched in fluxing compounds (e.g., Breiter et al. 2017; Harlaux
661 et al. 2018a; Xie et al. 2018; Yin et al. 2019), which might also record the processes of
662 tungsten mineralization related to fluids during their evolution through the magmatic–
663 hydrothermal transition. Collectively, the external and magmatic fluids all facilitated the
664 tungsten mineralization. The overall scenario of the ore-forming processes for the
665 Xihuashan tungsten deposit is summarized as follows (Fig. 13):

666 1) The W and F were gradually concentrated in the magmatic fluids via magmatic
667 fractionation.

668 2) The W and F-rich magmatic fluids pooled in the granitic cupola and induced
669 greisenization. This process destabilized the polymeric tungstates to form WO_4^{2-} in the
670 fluids.

671 3) The pooled fluid flow might have been overpressured, eventually being
672 injected into the vein system.

673 4) Tungsten and the fluids would have migrated along faults and fractures with
674 tungsten being precipitated as vein-type wolframite at favorable sites when the W and
675 F-rich fluid was mixed with an external meteoric fluid.

676 Therefore, tungsten mineralization is closely related to the mixture of magmatic
677 and external fluids. Furthermore, the presence of siderite in the greisen and muscovite

678 granite indicates that the fluids are rich in Fe and Mn, which are ore-forming elements
679 generating metal complexes with WO_4^{2-} during the precipitation of wolframite.

680 The input of Fe and Mn in the fluids would be attributed to the reactions between
681 external CO_2-bearing fluid and host-rock (Lecumberri-Sanchez et al., 2017; Wang et al.
682 2020). In addition, the fluid boiling process might also take the role of triggering the
683 precipitation of wolframite, as the transport of volatile elements (e.g., CO_2, H^+) into
684 vapor phase changes the chemical composition of the fluid (Korges et al., 2018).

685

686 ## ACKNOWLEDGEMENTS

687 We thank C.Y. Li, Y. Liu and X.L. Tu for analytical assistance. We are also grateful
688 to Dr. M. Harlaux and an anonymous reviewer for their careful reviews and constructive
689 comments, which strongly improved the manuscript. This study was financially
690 supported by the National Key Research and Development Program of China (No.
691 2016YFC0600204) and National Natural Science Foundation of China (NSFC Projects
692 41625007, U1701641). This is contribution No. IS-xxxx from GIG-CAS.

693

694 ## REFERENCES CITED

695 Akoh, J.U., and Ogunleye, P.O. (2014) Mineralogical and geochemical evolution of
696 muscovite in the pegmatite group of the Angwan Doka area, Kokoona district: A
697 clue to petrogenesis and tourmaline mineralization potential. Journal of
698 geochemical exploration, 146, 89–104.

699 Audéta , A., Pettke, T., Heinrich, C.A., and Bodnar, R.J. (2008) The composition of

magmatic-hydrothermal fluids in barren and mineralized intrusions. Economic Geology, 103, 877–908.

Bau, M., and Möller, P. (1992) Rare earth element fractionation in metamorphogenic hydrothermal calcite, magnesite and siderite. Mineralogy and Petrology, 45(45), 231–246.

Bau, M. (1996) Controls on the fractionation of isovalent trace elements in magmatic and aqueous systems: Evidence from Y/Ho, Zr/Hf, and lanthanide tetrad effect. Contributions to Mineralogy and Petrology, 123, 323-333.

Bea, F., Pereira, M.D., and Stroh, A. (1994) Mineral/leucosome trace-element partitioning in a peraluminous migmatite (a laser ablation-ICP-MS study). Chemical Geology, 117(1–4), 291–312.

Breiter, K., Ďurišová, J., Hrstka, T., Korbelová, Z., Vaňková, M.H., Galiová, M.V., Kanicky, V., Rambousek, P., Knésl, I., Dobeš, P., and Dosbaba, M. (2017) Assessment of magmatic vs. metasomatic processes in rare-metal granites: A case study of the Cínovec/Zinnwald Sn-W-Li deposit, Central Europe. Lithos, 292–293, 198–217.

Buzgar, N., and Apopei, A.I. (2009) The Raman study of certain carbonates. Geologie. Tomul LV, 2, 97–112.

Buckley, H.A., and Woolley, A.R. (1990) Carbonates of the magnesite-siderite series from four carbonatite complexes. Mineralogical Magazine, 54(376), 413–418.

Castorina, F., and Masi, U. (2008) REE and Nd-isotope evidence for the origin of siderite from Jebel Awan deposit (Central Morocco). Ore Geology Reviews, 34,

337-342.

Chang, H.L., and Huang, H.L. (2002) A preliminary investigation of melt inclusions and genesis of Xihuashan tungsten deposit. Acta Petrologica et Mineralogica, 21(2), 143-150 (in Chinese with English abstract).

Che, X.D., Linnen, R.L., Wang, R.C., Aseri, A., and Thibault, Y. (2013) Tungsten solubility in evolved granitic melts: An evaluation of magmatic wolframite. Geochimica et Cosmochimica Acta, 106: 84–98.

Deng, X.D., Luo, T., Li, J.W. and Hu, Z.C., (2019) Direct dating of hydrothermal tungsten mineralization using in situ wolframite U–Pb chronology by laser ablation ICP-MS. Chemical Geology, 515, 94–104.

El Korh, A., Boiron, M.C., Cathelineau, M., Deloule, E., and Luais, B. (2020) Tracing metallic pre-concentrations in the Limousin ophiolite-derived rocks and Variscan granites (French Massif Central). Lithos, 356, 105345.

Foster, M.D. (1960) Interpretation of the composition of trioctahedral micas. US Geological Survey Professional Paper, 354-E, 115–147.

Fusswinkel, T., Wagner, T., Wenzel, T., Wälle, M., and Lorenz, J. (2013) Evolution of unconformity-related MnFeAs vein mineralization, Sailauf (Germany): Insight from major and trace elements in oxide and carbonate minerals. Ore Geology Reviews, 50, 28–51.

Gleeson, S.A., Wilkinson, J.J., Stuart, F.M., and Banks, D.A. (2001) The origin and evolution of base metal mineralizing brines and hydrothermal fluids, South Cornwall, UK. Geochimica et Cosmochimica Acta, 65, 2067–2079.

Guo, C.L., Chen, Y.C., Zeng, Z.L., and Lou, F.S. (2012) Petrogenesis of the Xihuashan

granites in southeastern China: Constraints from geochemistry and in-situ analyses of zircon U-Pb-Hf-O isotopes. Lithos, 148, 209–227.

Harlaux, M., Mercadier, J., Marignac, C., Peiffert, C., Gloquet, C., and Cuney, M. (2018a) Tracing metal sources in peribatholitic hydrothermal W deposits based on the chemical composition of wolframite: The example of the Variscan French Massif Central. Chemical Geology, 479, 58–85.

Harlaux, M., Romer, R.L., Mercadier, J., Morlot, C., Marignac, C., and Cuney, M. (2018b) 40 Ma of hydrothermal W mineralization during the Variscan orogenic evolution of the French Massif Central revealed by U-Pb dating of wolframite. Mineralium Deposita, 53(1), 21–51.

Harlaux, M., Mercadier, J., Bonzi, W.M.E., Kremer, V., Marignac, C. and Cuney, M. (2017) Geochemical signature of magmatic-hydrothermal fluids exsolved from the Beauvoir rare-metal granite (Massif Central, France): insights from LA-ICPMS analysis of primary fluid inclusions. Geofluids, 1925817, 1-25.

Higgins, N.C. (1980) Fluid inclusion evidence for the transport of tungsten by carbonate complexes in hydrothermal solutions. Canadian Journal of Earth Sciences, 17, 823–830.

Hovis, G.L., Delbove, F., and Bose, M.R. (1991) Gibbs energies and entropies of K–Na mixing for alkali feldspars from phase equilibrium data: implications for feldspar solvi and short-range order. American Mineralogist, 76, 913–927.

Hu, R.Z., Bi, X.W., Jiang, G.H., Chen, H.W., Peng, J.T., Qi, Y.Q., Wu, L.Y., and Wei, W.F. (2012) Mantle-derived noble gases in ore-forming fluids of the granite-related Yaogangxian tungsten deposit, Southeastern China. Mineralium Deposita, 47, 623–

632.

Huang, H.L., Chang, H.L., Fu, J.M., Wang, X.W., and Li, T.Y. (2006) Formation pressure of wolframite-vein deposits and emplacement depth of related granite in Xihuashan, Jiangxi Province. Mineral Deposits, 25(5), 562–571 (in Chinese with English abstract).

Huang, H.L., Chang, H.L., Li, F., Tan, J., Zhang, C.H., Zhou, Y., Yang, K., and Yan, F. (2013) Microthermometry and characteristic element determination for the fluid inclusions in the wolframite and quartz in the drusy cavities of Xihuashan tungsten deposit. Earth Science Frontiers, 20(2), 205–212 (in Chinese with English abstract).

Hulsbosch, N., Boiron, M., Dewaele, S., and Muchez, P. (2016) Fluid fractionation of tungsten during granite–pegmatite differentiation and the metal source of peribatholitic W quartz veins: Evidence from the Karagwe-Ankole Belt (Rwanda). Geochimica et Cosmochimica Acta, 175, 299–318.

Irber, W. (1999) The lanthanide tetrad effect and its correlation with K/Rb, Eu/Eu*, Sr/Eu, Y/Ho, and Zr/Hf of evolving peraluminous granite suites. Geochimica et Cosmochimica Acta, 63(3–4), 489–508.

Jochum, K.P., Weis, U., Stoll, B., Kuzmin, D., Yang, Q., Raczek, I., Jacob, D.E., Stracke, A., Birbaum, K., Frick, D.A., and Günther, D. (2011) Determination of reference values for NIST SRM 610–617 glasses following ISO guidelines. Geostandards and Geoanalytical Research, 35(4), 397–429.

Keppler, H., and Wyllie, P.J. (1991) Partitioning of Cu, Sn, Mo, W, U, and Th between melt and aqueous fluid in the systems haplogranite-H_2O–HCl and

haplogranite-H_2O-HF. Contribution to Mineralogy and Petrology, 109, 139–150.

Korges M, Weis P, Lüders V, Laurent O. (2018) Depressurization and boiling of a single magmatic fluid as a mechanism for tin-tungsten deposit formation. Geology 46: 75-78.

Launay, G., Sizaret, S., Guillou-Frottier, L., Gloaguen, E., and Pinto, F. (2018) Deciphering fluid flow at the magmatic-hydrothermal transition: A case study from the world-class Panasqueira W–Sn–(Cu) ore deposit (Portugal). Earth and Planetary Science Letters, 499, 1–12.

Le Bel, L., Li, Y.D., and Sheng, J.F. (1984) Granitic evolution of the Xihuashan-Dangping (Jiangxi, China) tuntgsten-bearing system. Tschermaks Mineralogische und Petrographische Mitteilungen, 33, 149–167.

Lecumberri-Sanchez P, Vieira R, Heinrich CA, Pinto F, Wälle M. (2017) Fluid-rock interaction is decisive for the formation of tungsten deposits. Geology 45: 579-582.

Legros, H., Marignac, C., Mercadier, J., Cuney, M., Richard, A., Wang, R.C., Charles, N., and Lespinasse, M. (2016) Detailed paragenesis and Li-mica compositions as recorders of the magmatic-hydrothermal evolution of the Maoping W-Sn deposit (Jiangxi, China). Lithos, 264, 108–124.

Legros, H., Marignac, C., Tabary, T., Mercadier, J., Richard, A., Cuney, M., Wang, R.C., Charles, N., and Lespinasse, M. (2018) The ore-forming magmatic-hydrothermal system of the Piaotang W-Sn deposit (Jiangxi, China) as seen from Li-mica geochemistry. American Mineralogist, 103(1), 39–54.

Legros, H., Richard, A., Tarantola, A., Kouzmanov, K., Mercadier, J., Vennemann, T., Marignac, C., Cuney, M., Wang, R.C., Charles, N., and Bailly, L. (2019) Multiple fluids involved in granite-related W-Sn deposits from the world-class Jiangxi province (China). Chemical Geology, 508, 92–115.

Legros, H., Harlaux, M., Mercadier, J., Romer, R.L., Poujol, M., Camacho, A., Marignac, C., Cuney, M., Wang, R.C., Charles, N., and Lespinasse, M.Y. (2020) The world-class Nanling metallogenic belt (Jiangxi, China): W and Sn deposition at 160 Ma followed by 30 my of hydrothermal metal redistribution. Ore Geology Reviews, 117, 103302.

Longerich, H.P., Jackson, S.E., and Günther, D. (1996) Laser ablation inductively coupled plasma mass spectrometric transient signal data acquisition and analyte concentration calculation. Journal of Analytical Atomic Spectrometry, 11, 899–904.

Li, J., Huang, X.L,, He, P.L., Li, W.X., Yu, Y., and Chen, L.L. (2015) In situ analyses of micas in the Yashan granite, South China: constraints on magmatic and hydrothermal evolutions of W and Ta-Nb bearing granites. Ore Geology Reviews, 65, 793–810.

Li, J., Huang, X.L., Wei, G.J., Liu, Y., Ma, J.L., Han, L., and He, P.L. (2018) Lithium isotopic fractionation during magma differentiation and hydrothermal processes in the rare-metal granites. Geochimica et Cosmochimica Acta, 240, 64–79.

Li, Q.L., Li, X.H., Lan, Z.W., Guo, C.L., Yang, Y.N., Liu, Y., and Tang, G.Q. (2013) Monazite and xenotime U–Th–Pb geochronology by ion microprobe: dating highly fractionated granites at Xihuashan tungsten mine, SE China. Contributions to

833 Mineralogy and Petrology, 166, 65–80.

834 Liu, X.C, Xing, H.L., and Zhang, D.H. (2017) Influences of hydraulic fracturing on
835 fluid flow and mineralization at the vein-type tungsten deposits in southern China.
836 Geofluids, 4673421, 1-11.

837 Li, X.H., Li, W.X., Li, Z.X., Lo, C.H., Wang, J., Ye, M.F., and Yang, Y.H. (2009)
838 Amalgamation between the Yangtze and Cathaysia Blocks in South China:
839 constraints from SHRIMP U–Pb zircon ages, geochemistry and Nd–Hf isotopes of
840 the Shuangxiwu volcanic rocks. Precambrian Research, 174, 117–128.

841 Li, Z.X., Li, X.H., Wartho, J.A., Clark, C., Li, W.X., Zhang, C.L., and Bao, C. (2010)
842 Magmatic and metamorphic events during the early Paleozoic Wuyi-Yunkai
843 orogeny, southeastern South China: New age constraints and pressure-temperature
844 conditions. Geological Society of America Bulletin, 122(5–6), 772–793.

845 Lin, W.W., and Peng, L.J. (1994) The estimation of Fe^{3+} and Fe^{2+} contents in amphibole
846 and biotite from EPMA data. Journal of Changchun University of Science and
847 Technology, 24(2), 155–162 (in Chinese with English abstract).

848 Linnen, R.L., and Williams-Jones, A.E. (1995) Genesis of a magmatic metamorphic
849 hydrothermal system; the Sn-W polymetallic deposits at Pilok, Thailand. Economic
850 Geology, 90, 1921–1935.

851 Linnen, R.L. and Cuney, M. (2005) Granite-related rare-element deposits and
852 experimental constraints on Ta–Nb–W–Sn–Zr–Hf mineralization. In Rare-Element
853 Geochemistry and Mineral Deposits. GAC Short Course Notes, vol. 17 (eds. R. L.
854 Linnen and I. M. Samson). Geological Association of Canada, pp, 45–67.

855 Liu, J.Y. (2005) Composition of Xihuashan granites and its relationship to tungsten
856 metallogenesis. Contributions to Geology and Mineral Resources Research, 20, 1–7
857 (in Chinese with English abstract).
858 Liu, Y.S., Hu, Z.C., Gao, S., Gunther, D., Xu, J., Gao, C.G., and Chen, H.H. (2008) In
859 situ analysis of major and trace elements of anhydrous minerals by LA-ICP-MS
860 without applying an internal standard. Chemical Geology, 257, 34–43.
861 Ma, W.W., Huang, X.L., Yu, Y., Yin, R., and He, P.L. (2020) Characteristics of micas in
862 the Limu granite, South China: illuminating the hydrothermal processes related to
863 tin mineralization. Geotectonica et Metallogenia, (accepted, in Chinese with
864 English abstract).
865 Maruéjol, P., Cuney, M., and Turpin, L. (1990) Magmatic and hydrothermal R.E.E.
866 fractionation in the Xihuashan granites (SE China). Contributions to Mineralogy
867 and Petrology, 104, 668–680
868 Michard, A. (1989) Rare earth elements systematics in hydrothermal fluids. Geochimica
869 et Cosmochimica Acta, 53, 745–750.
870 Möller, P., Dulski, P., Savascin, Y., and Conrad, M. (2004) Rare earth elements, yttrium
871 and Pb isotope ratios in thermal spring and well waters of West Anatolia, Turkey: a
872 hydrothermal study of their origin. Chemical Geology, 206, 97–118.
873 Monier, G., and Robert, J.L. (1986) Muscovite solid solutions in the system
874 K_2O-MgO-FeO-Al_2O_3-SiO_2-H_2O: an experimental study at 2 kbar P_{H2O} and
875 comparison with natural Li-free white micas. Mineralogical Magazine, 50, 257–
876 266.

Mu, Z., Huang, F., Chen, C., Zheng, S., Fen, S., Lu, D., and Mei, Y. (1982) Oxygen, hydrogen and carbon isotope studies of Piaotang and Xihuashan quartz vein-type tungsten deposits, Jiangxi Province. In: Hepworth JV, Yu HZ (eds) Symposium on Tungsten geology, Jiangxi, China. ESCAP-RMRDC, Bandung, pp, 553–566.

Munoz, J.L. (1984) F-OH and Cl-OH exchange in micas with application to hydrothermal ore deposits. Reviews in Mineralogy, 13, 469–493.

Nie, R.F., and Wang, X.D. (2007) On research advancement of Gannan tungsten deposit. China tungsten industry 22(3), 1–5 (in Chinese with English abstract).

Pei, F.R., and Hong, D.W. (1995) New advances in the study of collision orogeny of granites in South China and their metallogenic series. Mineralium Deposita, 14(2), 189–194 (in Chinese).

Roda-Robles, E., Keller, P., Pesquera, A., and Fontan, F. (2007) Micas of the muscovite–lepidolite series from Karibib pegmatites, Namibia. Mineralogical Magazine, 71, 41–62.

Rudnick, R.L., and Gao, S. (2003) Composition of the continental crust. Treatise on Geochemistry, 3, 1–64

Sinclair, W.D., Gonevchuk, G.A., Korostelev, P.G., Semenyak, B I., Rodionov, S.M., Seltmann, R., and Stemprok, M. (2014) World Tin and Tungsten Deposit database; Geological Survey of Canada, Open File 7688, 1 .zip file. doi:10.4095/295581

Schaltegger, S., Pettke, T., Audétat, A., Reusser, E., and Heinrich, C.A. (2005) Magmatic-to-hydrothermal crystallization in the W–Sn mineralized Mole Granite (NSW, Australia): Part I: Crystallization of zircon and REE-phosphates over three

million years - a geochemical and U–Pb geochronological study. Chemical Geology, 220, 215–235.

Schwinn, G., and Markl, G. (2005) REE systematics in hydrothermal fluorite. Chemical Geology, 216, 225–248.

Simons, B., Andersen, J.C., Shail, R.K., and Jenner, F.E. (2017) Fractionation of Li, Be, Ga, Nb, Ta, In, Sn, Sb, W and Bi in the peraluminous Early Permian Variscan granites of the Cornubian Batholith: precursor processes to magmatic-hydrothermal mineralisation. Lithos, 278, 491–512.

Štemprok, M. (1990) Solubility of tin, tungsten and molybdenum oxides in felsic magmas. Mineralium Deposita, 25, 205–212.

Tang, Y., Cui, K., Zheng, Z., Gao, J., Han, J., Yang, J., and Liu, L. (2020) LA-ICP-MS U-Pb geochronology of wolframite by combining NIST series and common lead-bearing MTM as the primary reference material: Implications for metallogenesis of South China. Gondwana Research, *DOI: 10.1016/j.gr.2020.02.006.*

Taylor, S.R., and Mclennan, S.M. (1985) The continental crust: its composition and evolution, an examination of the geochemical record preserved in sedimentary rocks. Journal of Geology, 94(4), 632–633.

Tischendorf, G., Gottesmann, B., Foerster, H.J., and Trumbull, R.B. (1997) On Li-bearing micas: estimating Li from electron microprobe analyses and an improved diagram for graphical representation. Mineralogical Magazine, 61, 809–834.

Thomas, R., Förster, H., Rickers, K., and Webster, J.D. (2005) Formation of extremely F-rich hydrous melt fractions and hydrothermal fluids during differentiation of

highly evolved tin-granite magmas: a melt/fluid-inclusion study. Contributions to Mineralogy and Petrology, 148(5), 582–601.

Vallance, J., Cathelineau, M., Marignac, C., Boiron, M.C., Fourcade, S., Martineau, F., and Fabre, C. (2001) Microfracturing and fluid mixing in granites: W-(Sn) ore deposition at Vaulry (NW French Massif Central). Tectonophysics, 336, 43–61.

Van, Lichtervelde. M., Grégoire, M., Linnen, R.L., Béziat, D., and Salvi, S. (2008) Trace element geochemistry by laser ablation ICP-MS of micas associated with Ta mineralization in the Tanco pegmatite, Manitoba, Canada. Contribution to Mineralogy and Petrology, 155, 791–806.

Vigneresse, J.L. (2006) Element mobility in melts during successive intrusions of crustal-derived magmas and Sn-W mineralization. Resource Geology, 56(3), 293–314.

Vindel, E., Lopez, J.A., Boiron, M.C., Cathelineau, M., and Prieto, A.C. (1995) P-V-T-X-fO_2 evolution from wolframite to sulphide depositional stages in intragranitic W-veins. An example from the Spanish Central System. European Journal of Mineralogist, 7, 675–688.

Wang, F.Y., Li, C.Y., Ling, M.X., Zhang, H., Sun, Y.L., and Sun, W.D. (2011) Geochronology of the Xihuashan Tungsten deposit in Southeastern China: constraints from Re–Os and U–Pb dating. Resource Geology, 61, 414–423.

Wang, L.K., Zhu, W.F., and Zhang, S.L. (1982) On the evolution of two petrogenetic and mineralized series of granites in South China. Geochimica, 4, 329–339 (in Chinese with English abstract).

945 Wang, R.C., Fontan, F., Chen, X.M., Hu, H., Liu, S.C., and Xu, S.J., (2003) Accessory
946 minerals in the Xihuashan Y-enriched granite complex. The Canadian Mineralogist,
947 41, 727–748.
948 Wang, X.L. Qiu, Y., Lu, J.M. Chou, I, Zhang, W.L., Li, G.L, Hu, W.X., Li, Z., and
949 Zhong, R.C. (2020) In situ Raman spectroscopic investigation of the hydrothermal
950 speciation of tungsten: Implications for the ore-forming process. Chemical Geology
951 532, 119299.
952 Wei, W.F., Hu, R.Z., Bi, X.W., Peng, J.T., Su, W., Song, S.Q., and Shi, S.H. (2012)
953 Infrared microthermometric and stable isotopic study of fluid inclusions in
954 wolframite at the Xihuashan tungsten deposit, Jiangxi province, China. Mineralium
955 Deposita, 47, 589–605.
956 Wei, W.F., Hu, R.Z., Peng, J.T., Bi, X.W., Song, S.Q., and Shi, S.H. (2011) Fluid mixing
957 in Xihuashan tungsten deposit, Southern Jiangxi Province: hydrogen and oxygen
958 isotope simulation analysis. Geochimica, 40(1), 45-55 (in Chinese with English
959 abstract).
960 Wones, D.R., and Eugster, H.R. (1965). Stability of biotite experiment, theory, and
961 application. American Mineralogist, 50, 1228–1272.
962 Yang, J.H., Peng, J.T., Hu, R.Z., Bi, X.W., Zhao, J.H., Fu, Y.Z., and Shen, N.P. (2013)
963 Garnet geochemistry of tungsten-mineralized Xihuashan granites in South China.
964 Lithos, 177, 79–90.
965 Yang, J.H., Kang, L.F., Peng, J.T., Zhong, H., Gao, J.F., and Liu, L. (2018) In-situ
966 elemental and isotopic composition of apatite and zircon from the Shuikoushan and

Xihuashan granitic plutons: Implication for Jurassic granitoid-related Cu-Pb-Zn and W mineralization in the Nanling Range, South China. Ore Geology Reviews, 93, 382–403.

Yin, L., Pollard, P., Hu, S.X., and Taylor, R. (1995) Geologic and geochemical characteristics of the Yichun Ta-Nb-Li deposit, Jiangxi Province, South China. Economic Geology, 90, 577–585.

Yin, R., Han, L., Huang, X.L., Li, J., Li, W.X., and Chen, L.L. (2019) Textural and chemical variations of micas as indicators for tungsten mineralization: Evidence from highly evolved granites in the Dahutang tungsten deposit, South China. American Mineralogist, 104, 949–965.

Xie, L., Wang, R.C., Groat, L.A., Zhu, J.C., Huang, F.F., and Cempírek, J. (2015) A combined EMPA and LA-ICP-MS study of Li-bearing mica and Sn–Ti oxide minerals from the Qiguling topaz rhyolite (Qitianling District, China): The role of fluorine in origin of tin mineralization. Ore Geology Reviews, 65, 779–792.

Xie, L., Wang, R.C., Che, X.D., Huang, F.F., Erdmann, S., and Zhang, W.L. (2016) Tracking magmatic and hydrothermal Nb–Ta–W–Sn fractionation using mineral textures and composition: A case study from the late Cretaceous Jiepailing ore district in the Nanling Range in South China. Ore Geology Reviews, 78, 300–321.

Xie, L., Wang, Z., Wang, R., Zhu, J., Che, X., Gao, J., and Zhao, X. (2018) Mineralogical constraints on the genesis of W–Nb–Ta mineralization in the Laiziling granite (Xianghualing district, south China). Ore Geology Reviews, 95, 695–712.

989 Zhang, C., Holtz, F., Ma, C.Q., Wolff, P.E., and Li, X.Y. (2012) Tracing the evolution
990 and distribution of F and Cl in plutonic system from volatile-bearing minerals: a
991 case study from the Liujiawa pluton (Dabie orogeny, China). Contributions to
992 Mineralogy and Petrology, 164, 859–879.
993 Zhang, L., Zhuang, L., Qian, Y., Guo, Y., and Qu, P. (1982) Stable isotope geochemistry
994 of granites and tungsten tin deposit in Xihuashan-Piaotang area, Jiangxi Province.
995 In: Hepworth JV, Yu HZ (eds) Symposium on Tungsten geology, Jiangxi, China.
996 ESCAP-RMRDC, Bandung, pp, 553–566.
997 Zhao, J.H., Zhou, M.F., Yan, D.P., Zheng, J.P., and Li, J.W. (2011) Reappraisal of the
998 ages of Neoproterozoic strata in South China: no connection with the Grenvillian
999 orogeny. Geology, 39, 299–302.
1000 Zhou, X.M., Sun, T., Shen, W.Z., Shu, L.S., and Niu, Y.L. (2006) Petrogenesis of
1001 Mesozoic granitoids and volcanic rocks in South China: a response to tectonic
1002 evolution. Episodes, 29, 26–33.
1003 Zhu, C., and Sverjensky, D.A. (1992) F-Cl-OH partitioning between biotite and apatite.
1004 Geochimica et Cosmochimica Acta, 56, 3435–3467.
1005

FIGURE CAPTIONS

Fig. 1 (a) The distribution of granites and volcanic rocks of different ages in SE China (modified from Li et al. 2010), showing the locations of the Nanling W–Sn polymetallic mineralization region (NPMR) and the Xihuashan tungsten deposit. (b) Simplified geological map of the Xihuashan pluton (modified from Guo et al. 2012), showing four successive intrusions in the Xihuashan mining district (G1–G4, which correspond to coarse-grained biotite granite, medium-grained biotite granite, medium- to fine-grained biotite granite, and fine-grained biotite granite, respectively. After Wang et al. 2003).

Fig. 2 Hand specimen photographs (left) and photomicrographs (right) showing the petrography of the Xihuashan granites and greisen (in cross-polarized light) and the different micas encountered in this study. (a) Biotite granite. Biotite (siderophyllite) and associated apatite and ilmenite inclusions. (b) Two-mica granite. Biotite (lithian siderophyllite), muscovite and associated apatite and ilmenite inclusions; the rim of the biotite was eroded, as shown by the irregular embayed form. (c) Muscovite granite. Muscovite is present between the feldspar (both plagioclase and K-feldspar) and quartz. (d) Greisen. Biotite (lithian siderophyllite) and Li-mica occur between quartz grains. Mineral abbreviations: K-feldspar (Kfs), plagioclase (Pl), quartz (Qtz), biotite (Bt), muscovite (Ms), apatite (Ap), ilmenite (Ilm), zircon (Zrn), xenotime (Xtm).

Fig. 3 The diagrams of (a) TAS, (b) A/NK vs. A/CNK, and (c–h) TiO_2, MgO, P_2O_5, F, K_2O, and CaO contents versus Fe_2O_3 for the Xihuashan pluton. The total Fe in

the whole rock analyses is reported as Fe_2O_3. Plots I–IV from Guo et al. (2012) represent the data of different intrusions.

Fig. 4 Chondrite-normalized REE patterns and mean upper crust-normalized multi-element diagrams for rocks in the Xihuashan pluton. The chondrite and mean upper crust values are from Taylor and McLennan (1985) and Rudnick and Gao (2003), respectively. Data in shaded field are from Guo et al. (2012).

Fig. 5 (a-d) Back-scattered-electron (BSE) images of micas in different intrusions of the Xihuashan pluton; (e) and (f) representative BSE images of wolframite in greisen.

Fig. 6 Diagrams of TiO_2, Al_2O_3, FeO^{Tot}, MgO, F, and Cl contents versus SiO_2 for micas in the rocks of the Xihuashan pluton. BG = biotite granite, TMG = two-mica granite, and MG = muscovite granite.

Fig. 7 Diagrams of V, Cs, Rb, Nb, Ta, W, Sn, and Nb/Ta versus FeO^{Tot} + MnO + MgO contents for micas in the rocks of the Xihuashan pluton. The dashed lines connect the cores and corresponding rims of zoned mica. BG = biotite granite, TMG = two-mica granite, and MG = muscovite granite.

Fig. 8 (a) Representative BSE image, (b) Raman spectra, (c) chondrite-normalized REE patterns, and (d) mean upper crust-normalized multi-element diagrams for siderite in the Xihuashan muscovite granite and greisen. Chondrite and mean upper crust values are from Taylor and McLennan (1985) and Rudnick and Gao (2003), respectively.

Fig. 9 (a, b) Variation of measured Li_2O versus SiO_2 and F for micas in the rocks of

the Xihuashan pluton. The regression equations of (1) $Li_2O = 0.289 \times SiO_2 - 9.658$ and (2) $Li_2O = 0.3935 \times F^{1.326}$ from Tischendorf et al. (1997) can be applied to trioctahedral and dioctahedral micas, respectively. (c) Relationships between measured Li_2O and F in hydrothermal micas, which define a regression equation of (3) $Li_2O = 0.0748 \times F^2 + 0.0893 \times F$ that could be applied to the hydrothermal micas in our samples. (d) Comparison between measured and calculated Li_2O for micas in the rocks of the Xihuashan pluton. Some data for the hydrothermal micas were taken from previous studies (Van Lichtervelde 2008; Akoh and Ogunleye 2014; Xie et al. 2015; Yin et al. 2019; Ma et al. 2020). BG = biotite granite, TMG = two-mica granite, and MG = muscovite granite.

Fig. 10 (a) Variations in the compositions of mica from the Xihuashan pluton on the diagram of [Mg – Li] vs. [Fe^{Tot} + Mn + Ti – Al^{VI}] (according to Tischendorf et al. 1997). (b) Relationships between Li and octahedral cations (based on Foster 1960). The arrows indicate the trends in mica compositions due to magmatic evolution. The shadow area represents the field of the transitional series, known as the ferrous aluminous micas (Monier and Robert 1986). D.T. and T.T. denote the compositional trends of dioctahedral and trioctahedral micas, respectively. BG = biotite granite, TMG = two-mica granite, and MG = muscovite granite.

Fig. 11 Plots of (a) SiO_2 versus $\log(fH_2O/fHF)$, (b) Fe^{3+}/Fe^{2+} versus $\log(fH_2O/fHF)$, and (c) SiO_2 versus W_F^m for micas in the Xihuashan pluton. BG = biotite

granite, TMG = two-mica granite, and MG = muscovite granite.

Fig. 12 Plots of Rb, Cs, and W versus K/Rb for micas in the Xihuashan pluton. BG = biotite granite, TMG = two-mica granite, and MG = muscovite granite.

Fig. 13 Cartoon of tungsten mineralization in the Xihuashan pluton, illustrating the relationship between the evolution of the magmatic–hydrothermal system and the W mineralization. The spatial relationships between the bodies of granite and greisen are based on previous investigations (Liu 2005; Huang et al. 2006).

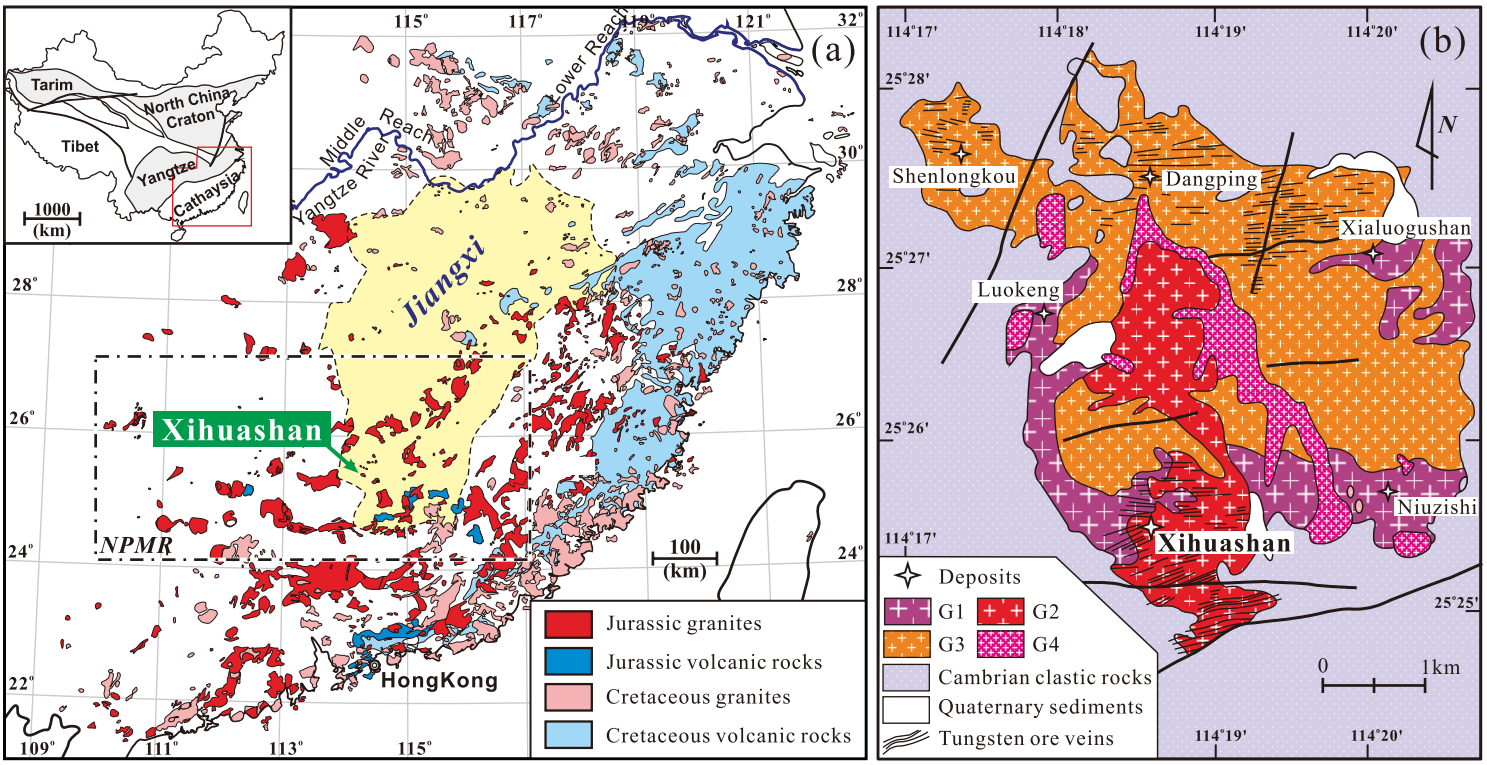
(a)
Tarim
North China Craton
Tibet
Yangtze
Cathaysia
1000 (km)
Middle Reach
Yangtze River
Lower Reach
Jiangxi
Xihuashan
NPMR
HongKong
100 (km)
Jurassic granites
Jurassic volcanic rocks
Cretaceous granites
Cretaceous volcanic rocks
115°
117°
119°
121°
32°
30°
28°
26°
24°
22°
109°
111°
113°
115°
(b)
114°17'
114°18'
114°19'
114°20'
25°28'
25°27'
25°26'
25°25'
N
Shenlongkou
Dangping
Xialuogushan
Luokeng
Niuzishi
Xihuashan
Deposits
G1
G2
G3
G4
Cambrian clastic rocks
Quaternary sediments
Tungsten ore veins
0
1km


(a)
CM

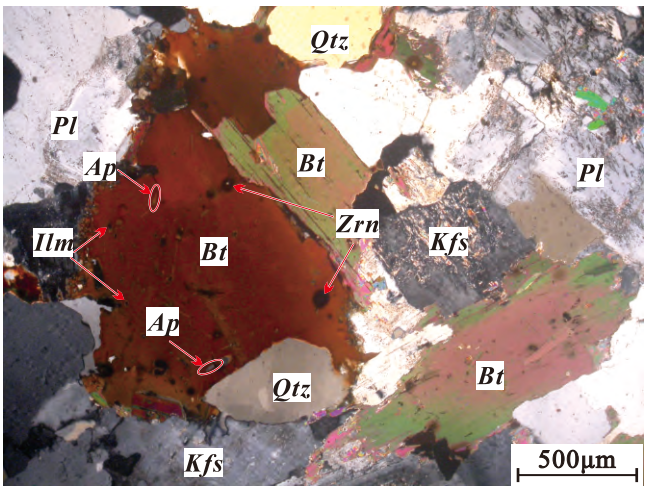
Qtz
Pl
Ap
Bt
Pl
Zrn
Ilm
Bt
Kfs
Ap
Qtz
Bt
Kfs
500μm


(b)
CM

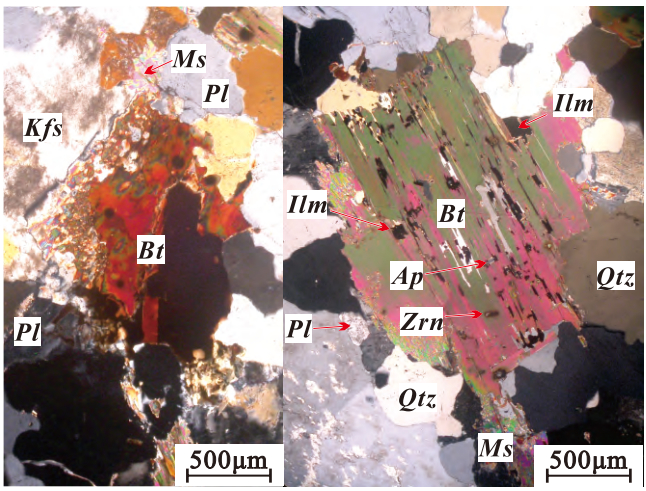
Ms
Pl
Kfs
Bt
Pl
500μm
Ilm
Ilm
Bt
Ap
Qtz
Pl
Zrn
Qtz
Ms
500μm


(c)
CM

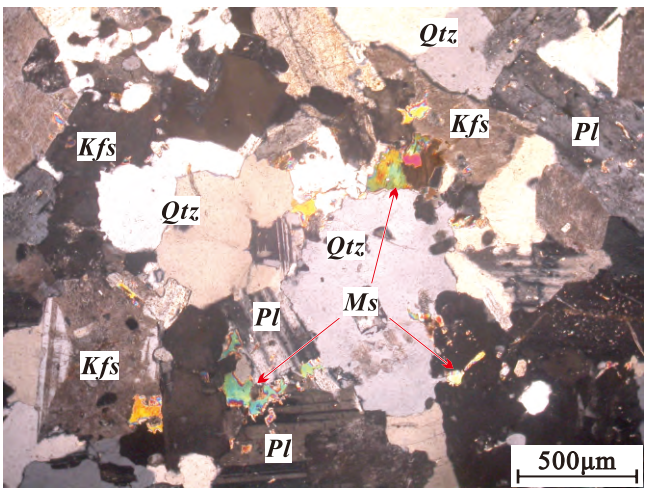
Qtz
Kfs
Kfs
Pl
Qtz
Qtz
Ms
Pl
Kfs
Pl
500μm


(d)
CM

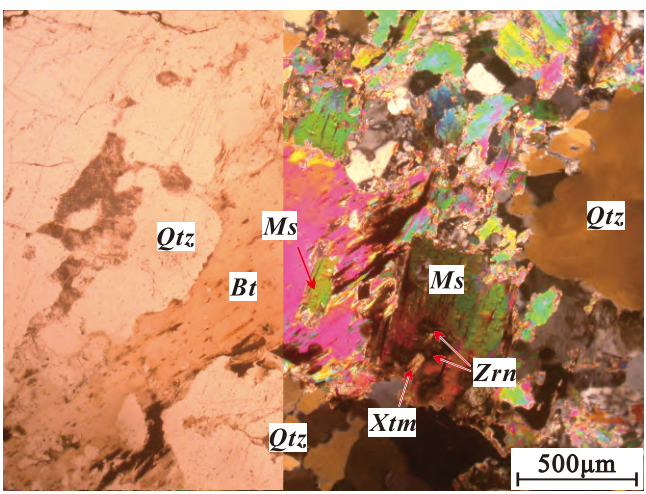
Qtz
Ms
Qtz
Bt
Ms
Zrn
Xtm
Qtz
500μm

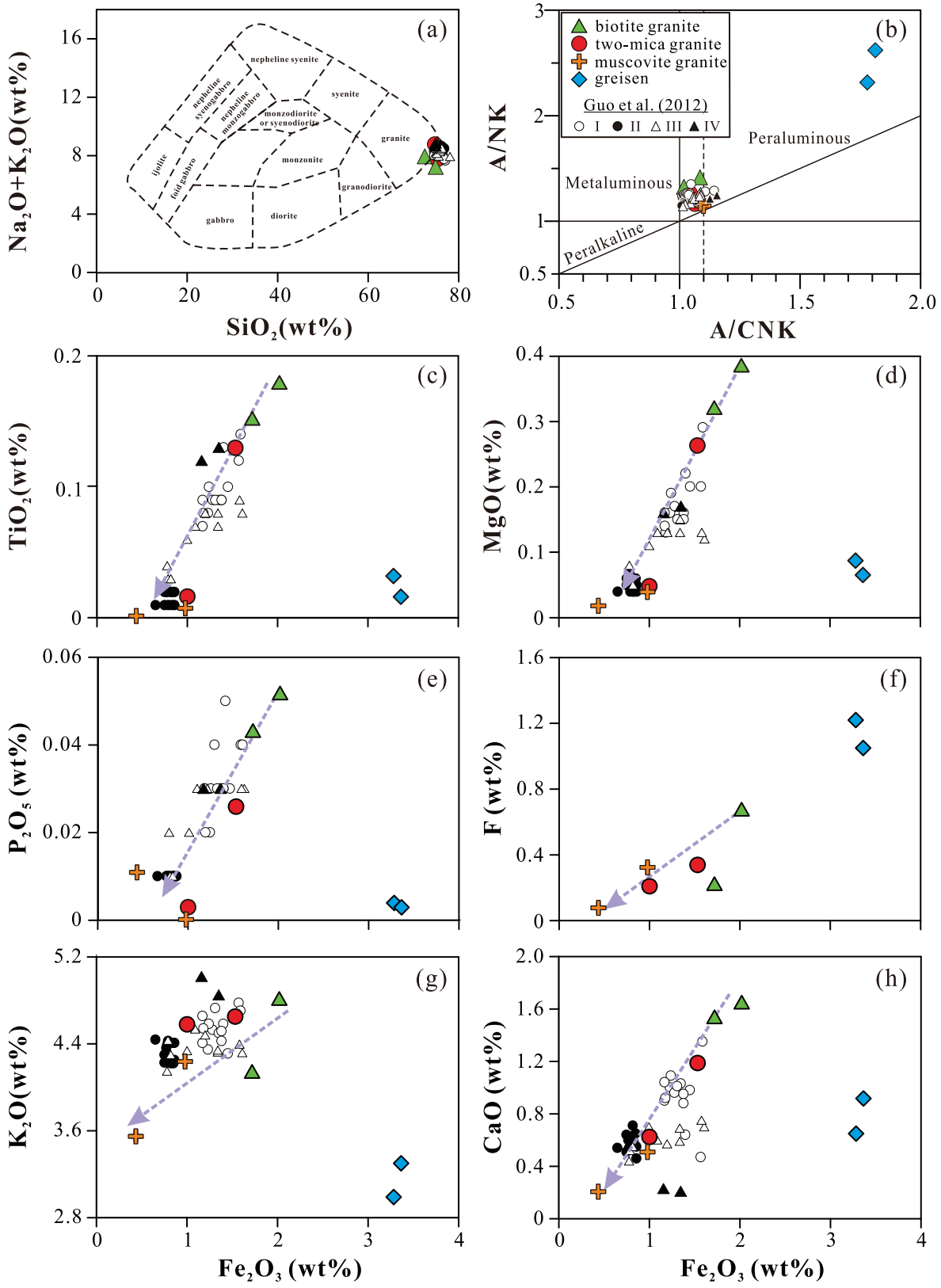
(a)
nepheline syenite
syenite
nepheline syenogabbro
nepheline monzogabbro
monzodiorite or syenodiorite
granite
ijolite
foid gabbro
monzonite
granodiorite
gabbro
diorite
Na2O+K2O(wt%)
SiO2(wt%)
(b)
biotite granite
two-mica granite
muscovite granite
greisen
Guo et al. (2012)
I II III IV
Peraluminous
Metaluminous
Peralkaline
A/NK
A/CNK
(c)
TiO2(wt%)
(d)
MgO(wt%)
(e)
P2O5 (wt%)
(f)
F (wt%)
(g)
K2O(wt%)
Fe2O3 (wt%)
(h)
CaO (wt%)
Fe2O3 (wt%)

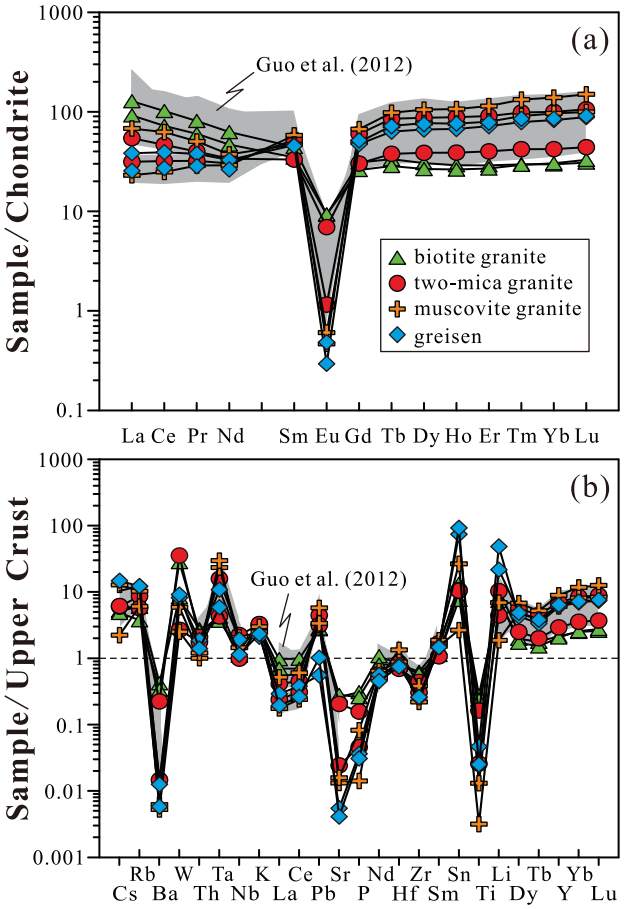
(a)
Guo et al. (2012)
Sample/Chondrite
1000
100
10
1
0.1
biotite granite
two-mica granite
muscovite granite
greisen
La Ce Pr Nd Sm Eu Gd Tb Dy Ho Er Tm Yb Lu
(b)
Guo et al. (2012)
Sample/Upper Crust
1000
100
10
1
0.1
0.01
0.001
Rb W Ta K Ce Sr Nd Zr Sn Li Tb Yb
Cs Ba Th Nb La Pb P Hf Sm Ti Dy Y Lu

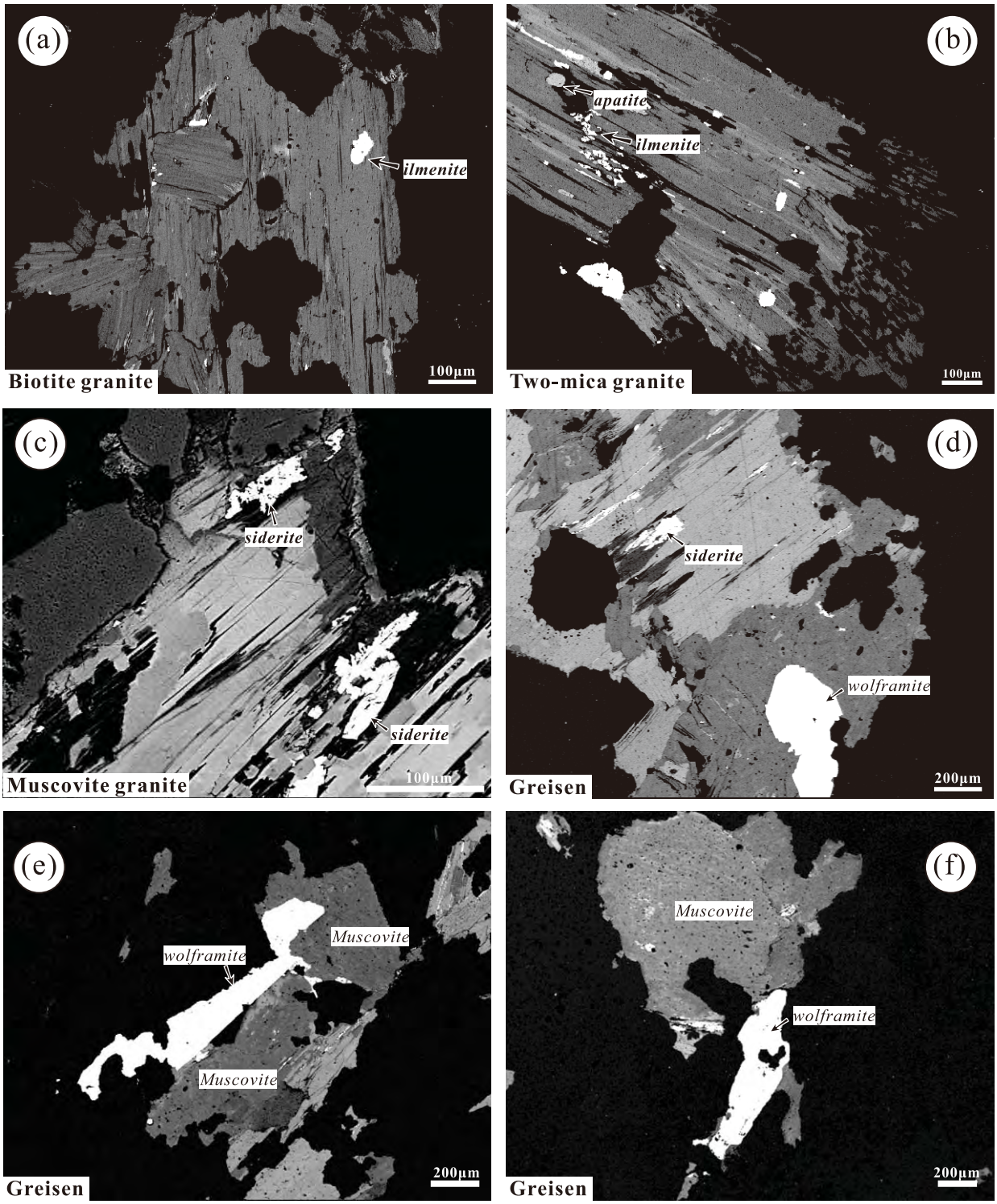
(a)
ilmenite
100μm
Biotite granite
(b)
apatite
ilmenite
100μm
Two-mica granite
(c)
siderite
siderite
100μm
Muscovite granite
(d)
siderite
wolframite
200μm
Greisen
(e)
Muscovite
wolframite
Muscovite
200μm
Greisen
(f)
Muscovite
wolframite
200μm
Greisen

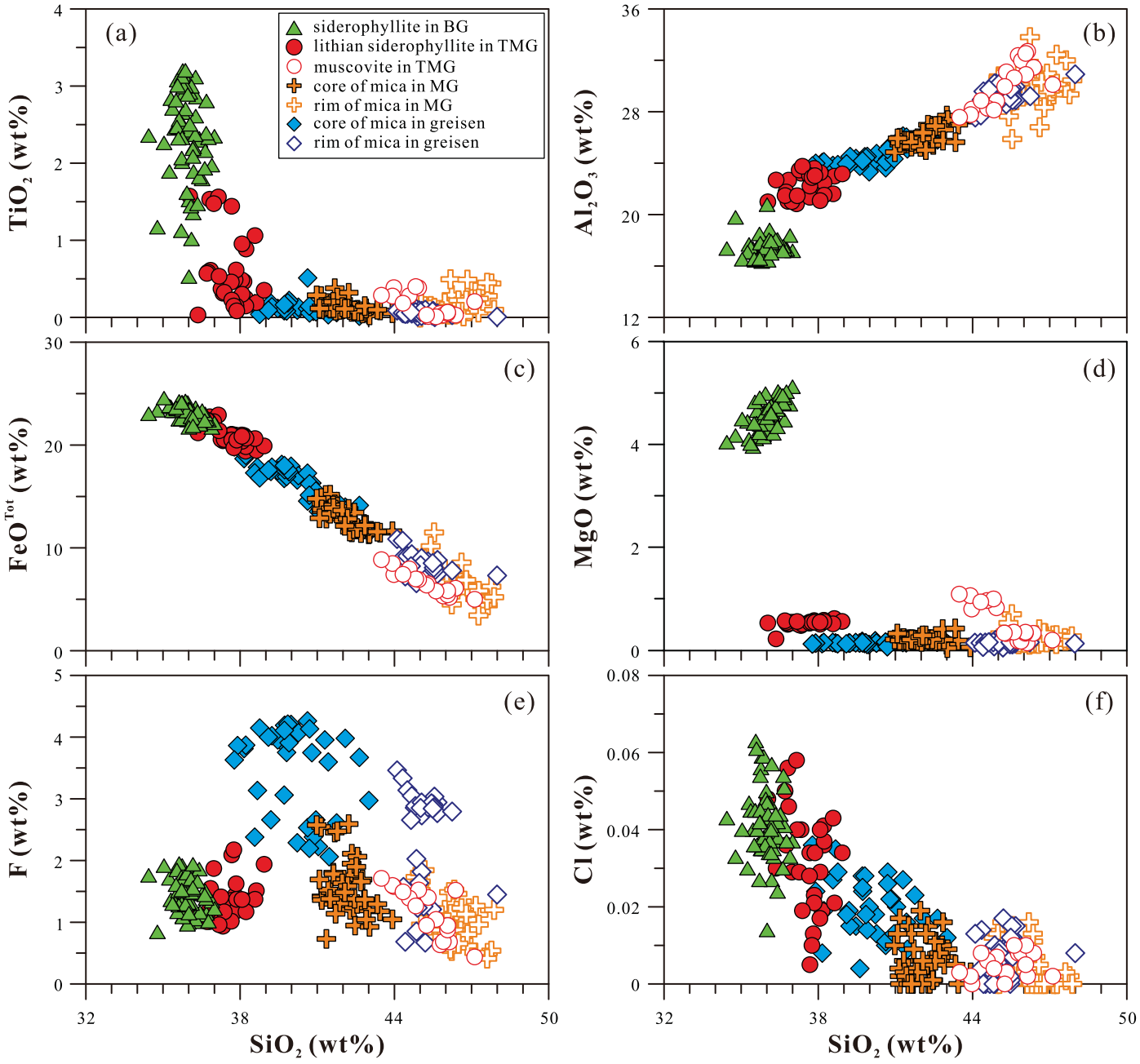
(a)
siderophyllite in BG
lithian siderophyllite in TMG
muscovite in TMG
core of mica in MG
rim of mica in MG
core of mica in greisen
rim of mica in greisen
TiO2 (wt%)
(b)
Al2O3 (wt%)
(c)
FeOTot (wt%)
(d)
MgO (wt%)
(e)
F (wt%)
(f)
Cl (wt%)
SiO2 (wt%)
SiO2 (wt%)

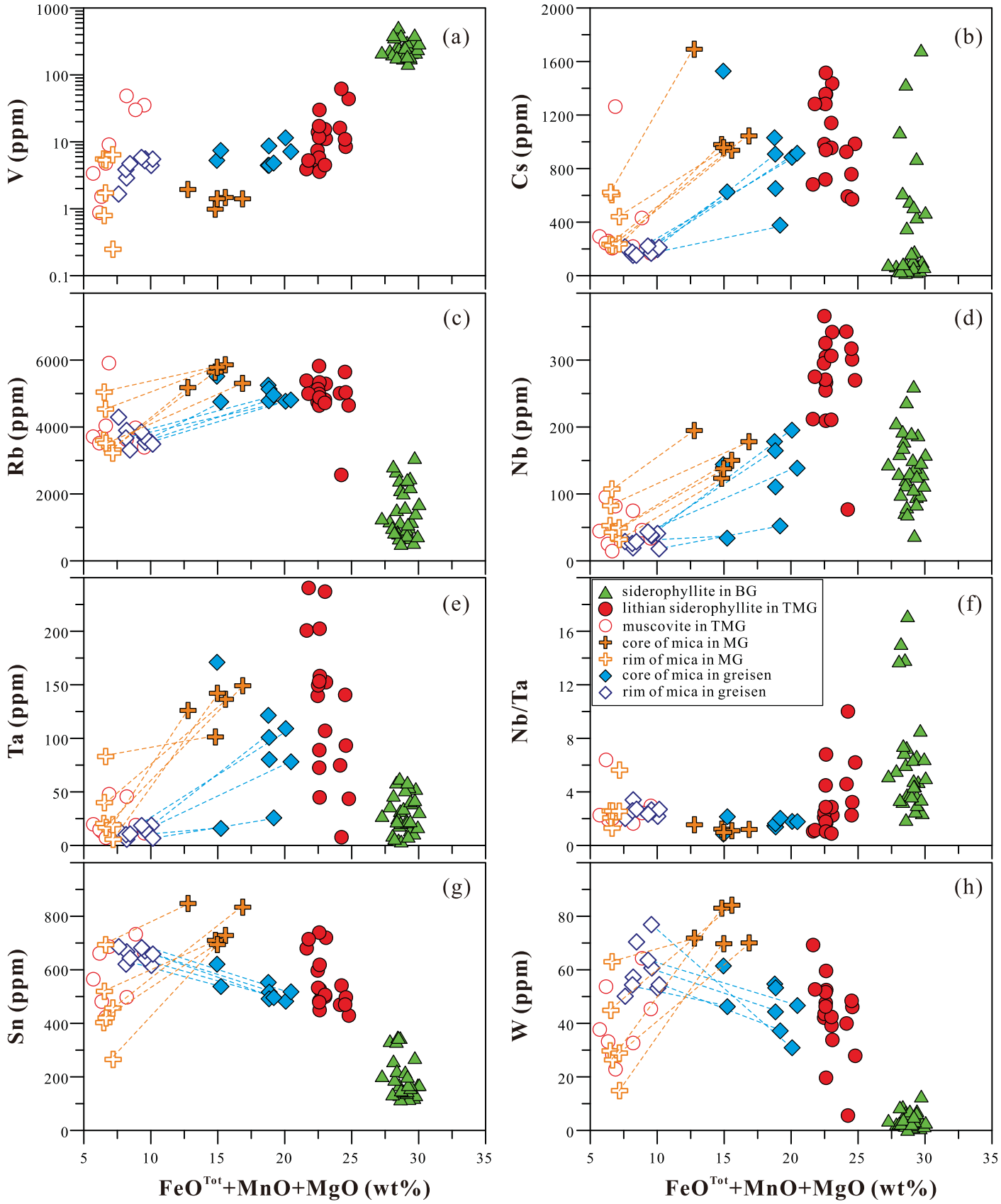
(a)
V (ppm)
1000
100
10
1
0.1
(b)
Cs (ppm)
2000
1600
1200
800
400
0
(c)
Rb (ppm)
6000
4000
2000
0
(d)
Nb (ppm)
300
200
100
0
(e)
Ta (ppm)
200
150
100
50
0
(f)
Nb/Ta
16
12
8
4
0
siderophyllite in BG
lithian siderophyllite in TMG
muscovite in TMG
core of mica in MG
rim of mica in MG
core of mica in greisen
rim of mica in greisen
(g)
Sn (ppm)
800
600
400
200
0
(h)
W (ppm)
80
60
40
20
0
5
10
15
20
25
30
35
FeO^Tot+MnO+MgO (wt%)
FeO^Tot+MnO+MgO (wt%)

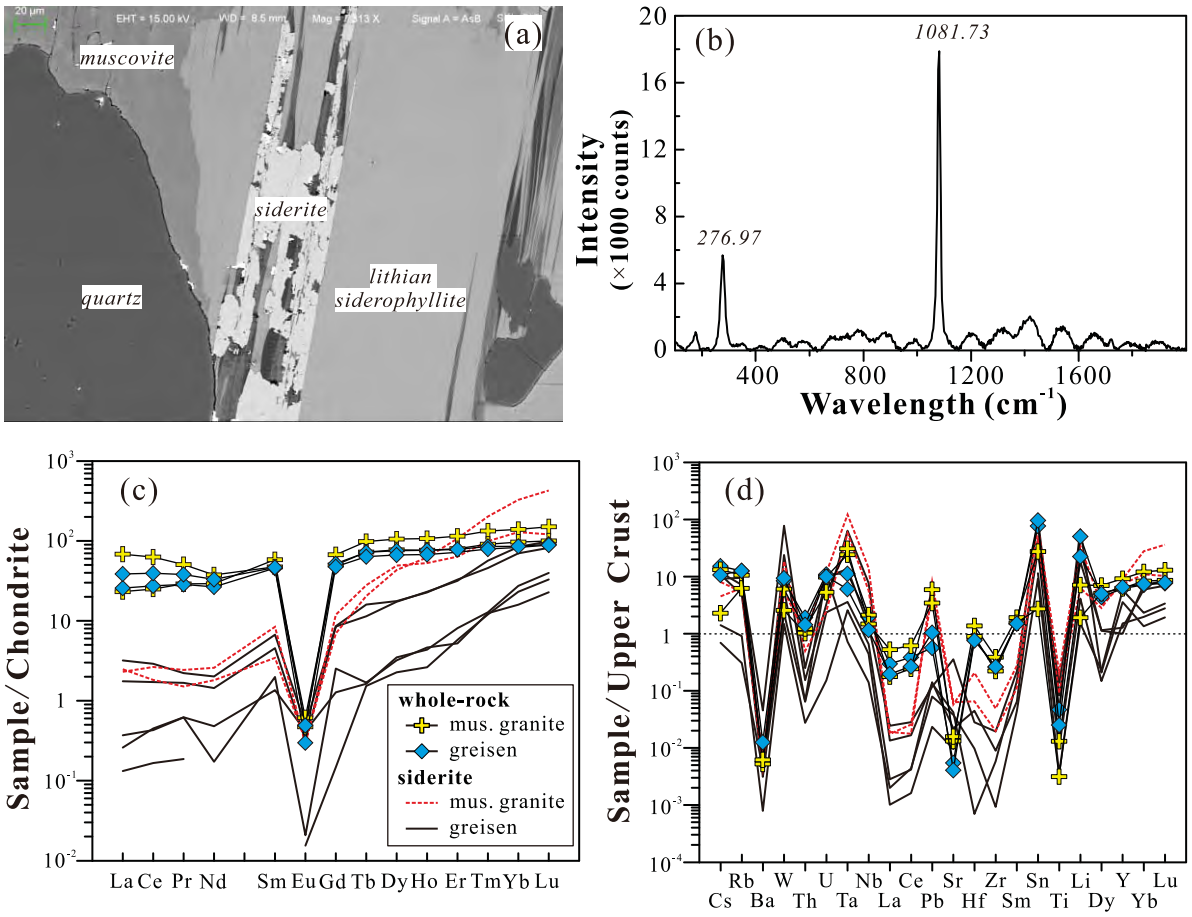
(a)
muscovite
siderite
quartz
lithian
siderophyllite
(b)
1081.73
276.97
Intensity
(×1000 counts)
Wavelength (cm-1)
(c)
Sample/Chondrite
whole-rock
mus. granite
greisen
siderite
mus. granite
greisen
La Ce Pr Nd Sm Eu Gd Tb Dy Ho Er Tm Yb Lu
(d)
Sample/Upper Crust
Rb Cs W Ba U Th Nb Ta Ce La Sr Pb Zr Hf Sn Sm Li Ti Y Dy Lu Yb

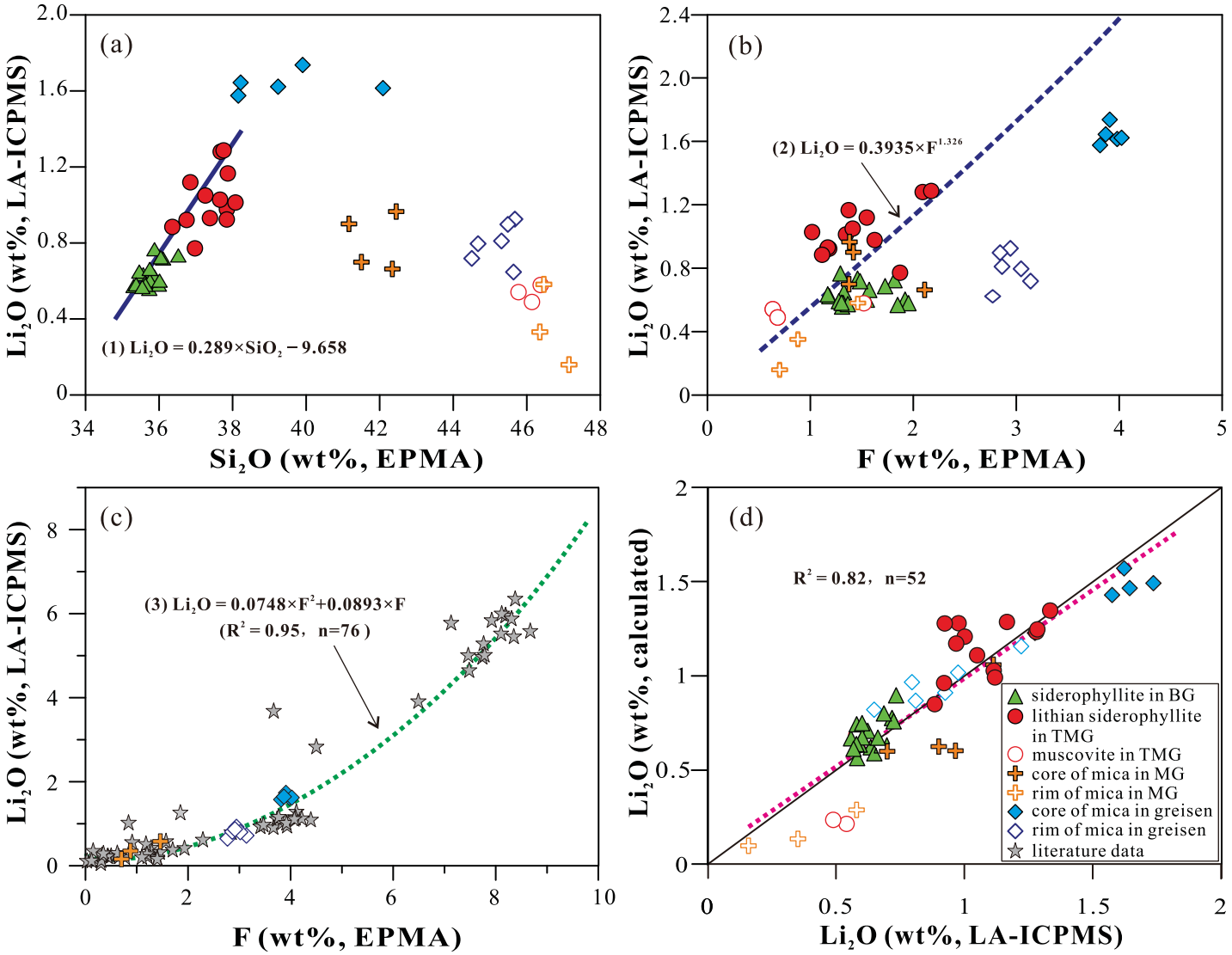
(a)
(1) $Li_2O = 0.289 \times SiO_2 - 9.658$
Li_2O (wt%, LA-ICPMS)
Si_2O (wt%, EPMA)
(b)
(2) $Li_2O = 0.3935 \times F^{1.326}$
Li_2O (wt%, LA-ICPMS)
F (wt%, EPMA)
(c)
(3) $Li_2O = 0.0748 \times F^2 + 0.0893 \times F$
($R^2 = 0.95$, n=76)
Li_2O (wt%, LA-ICPMS)
F (wt%, EPMA)
(d)
$R^2 = 0.82$, n=52
siderophyllite in BG
lithian siderophyllite in TMG
muscovite in TMG
core of mica in MG
rim of mica in MG
core of mica in greisen
rim of mica in greisen
literature data
Li_2O (wt%, calculated)
Li_2O (wt%, LA-ICPMS)

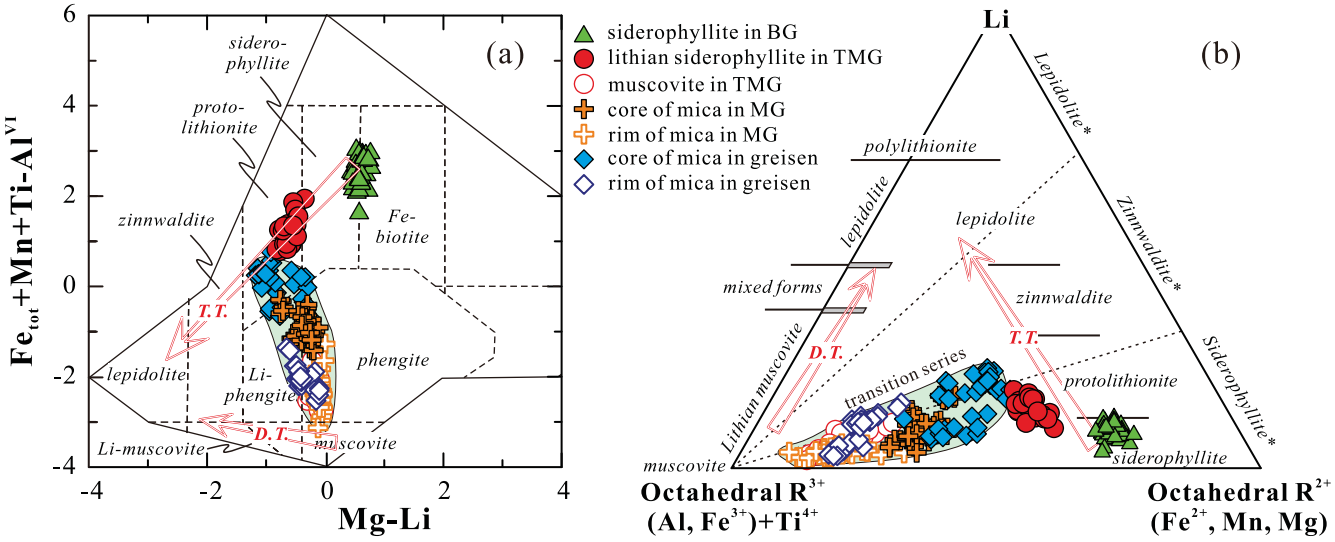
(a)
sidero-
phyllite
proto-
lithionite
zinnwaldite
Fe-
biotite
T.T.
lepidolite
Li-
phengite
phengite
D.T.
Li-muscovite
muscovite
Fe$_{tot}$+Mn+Ti-Al^{VI}
Mg-Li
siderophyllite in BG
lithian siderophyllite in TMG
muscovite in TMG
core of mica in MG
rim of mica in MG
core of mica in greisen
rim of mica in greisen
(b)
Li
Lepidolite*
polylithionite
lepidolite
Zinnwaldite*
mixed forms
lepidolite
zinnwaldite
T.T.
D.T.
Lithian muscovite
transition series
protolithionite
Siderophyllite*
muscovite
siderophyllite
Octahedral R^{3+}
(Al, Fe^{3+})+Ti^{4+}
Octahedral R^{2+}
(Fe^{2+}, Mn, Mg)

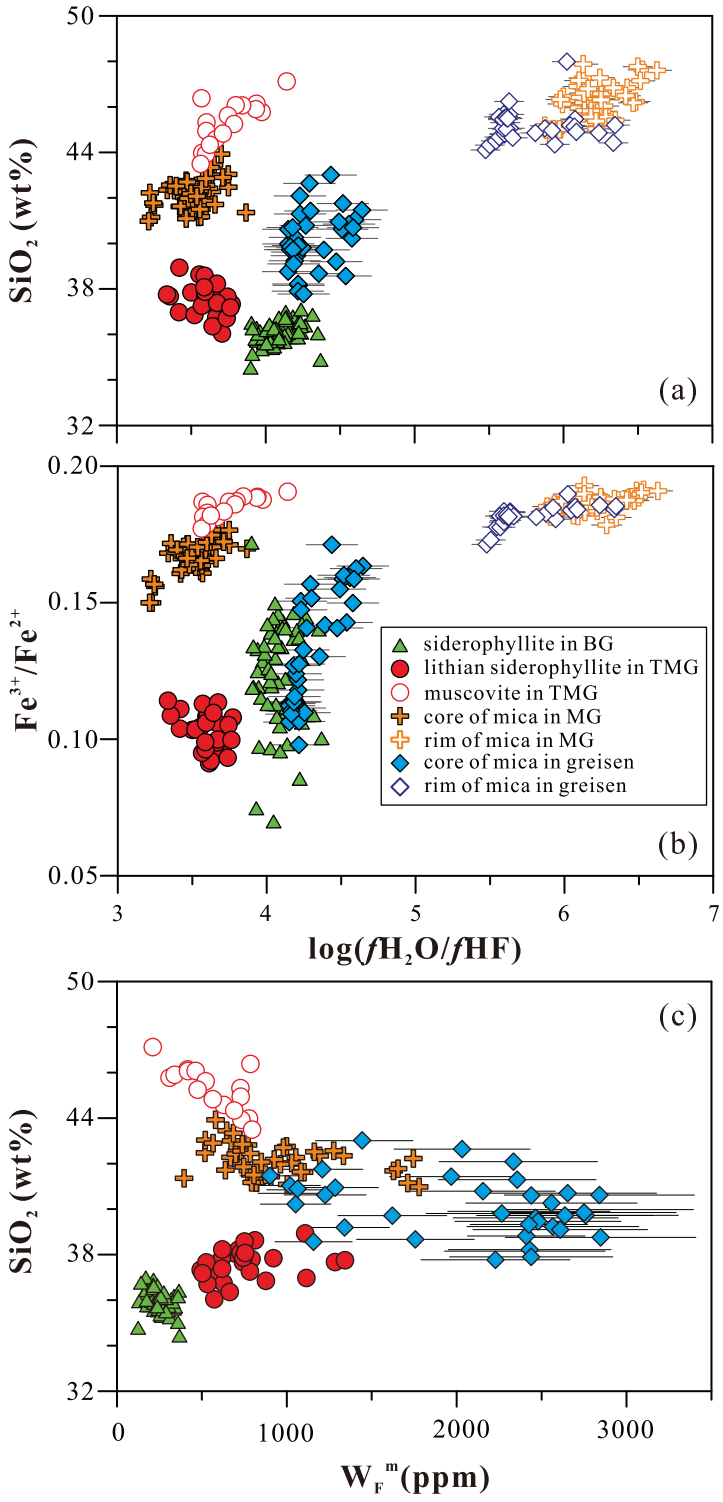
50
44
38
32
SiO2 (wt%)
(a)
0.20
0.15
0.10
0.05
Fe3+/Fe2+
siderophyllite in BG
lithian siderophyllite in TMG
muscovite in TMG
core of mica in MG
rim of mica in MG
core of mica in greisen
rim of mica in greisen
(b)
3
4
5
6
7
log(fH2O/fHF)
50
44
38
32
SiO2 (wt%)
(c)
0
1000
2000
3000
WFm(ppm)

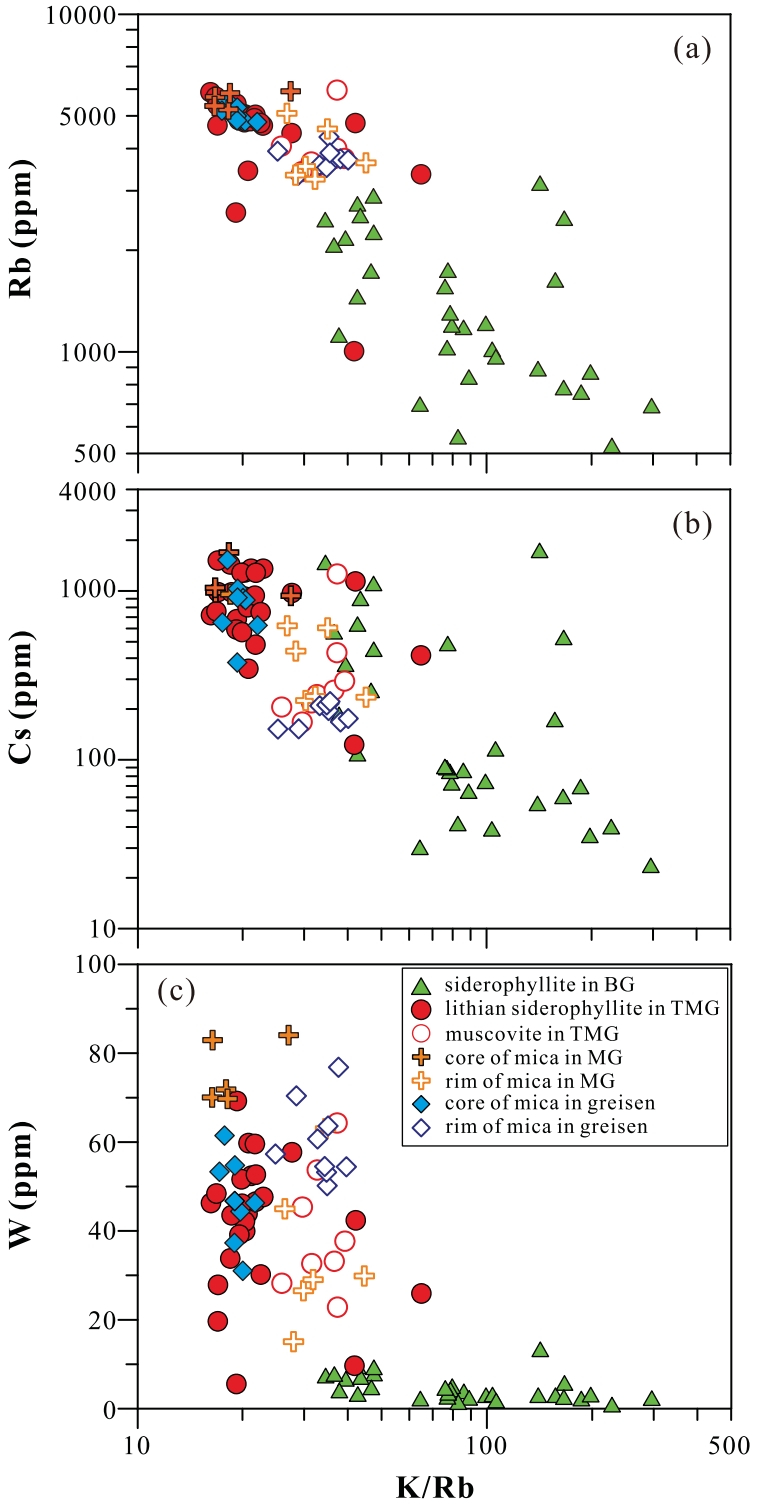
(a)
(b)
(c)
Rb (ppm)
Cs (ppm)
W (ppm)
K/Rb
10000
5000
1000
500
4000
1000
100
10
100
80
60
40
20
0
10
100
500
siderophyllite in BG
lithian siderophyllite in TMG
muscovite in TMG
core of mica in MG
rim of mica in MG
core of mica in greisen
rim of mica in greisen

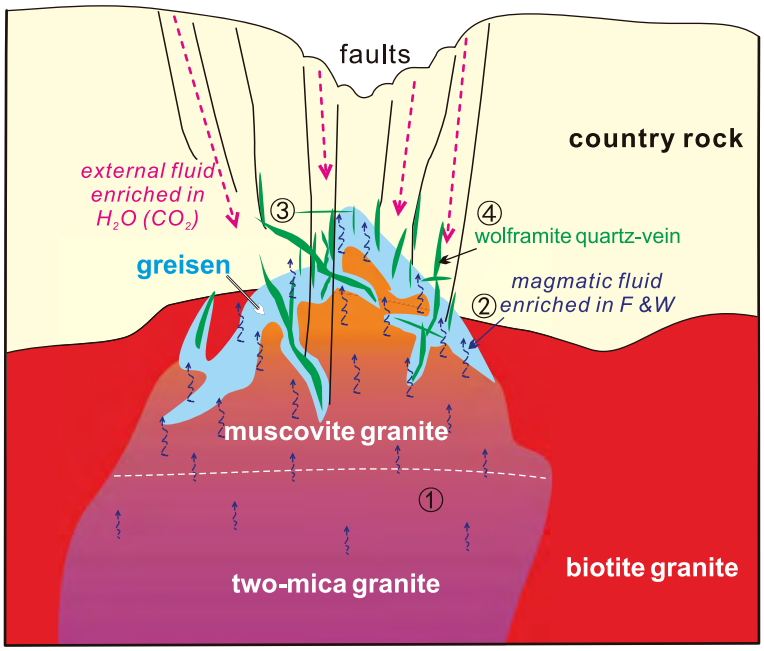
faults
country rock
external fluid
enriched in
H_2O (CO_2)
③
④
wolframite quartz-vein
greisen
magmatic fluid
②enriched in F &W
muscovite granite
①
two-mica granite
biotite granite